

# JGR Solid Earth

## RESEARCH ARTICLE

10.1029/2021JB022307

### Key Points:

- A forward model is presented to quantify seismic velocity and electrical conductivity of solid-liquid mixtures in crust-uppermost mantle
- The input parameters include pressure, temperature, lithology, liquid phase composition and fraction, and solid-liquid geometry
- For a given set of seismic velocity and electrical conductivity, the optimal parameter values can be found by inversion

### Supporting Information:

Supporting Information may be found in the online version of this article.

### Correspondence to:

H. Iwamori,  
hiwamori@eri.u-tokyo.ac.jp

### Citation:

Iwamori, H., Ueki, K., Hoshide, T., Sakuma, H., Ichiki, M., Watanabe, T., et al. (2021). Simultaneous analysis of seismic velocity and electrical conductivity in the crust and the uppermost mantle: A forward model and inversion test based on grid search. *Journal of Geophysical Research: Solid Earth*, 126, e2021JB022307. <https://doi.org/10.1029/2021JB022307>

Received 3 MAY 2021

Accepted 23 AUG 2021

## Simultaneous Analysis of Seismic Velocity and Electrical Conductivity in the Crust and the Uppermost Mantle: A Forward Model and Inversion Test Based on Grid Search

Hikaru Iwamori<sup>1</sup> , Kenta Ueki<sup>2</sup> , Takashi Hoshide<sup>3</sup> , Hiroshi Sakuma<sup>4</sup> , Masahiro Ichiki<sup>5</sup> , Tohru Watanabe<sup>6</sup> , Michihiko Nakamura<sup>7</sup> , Hitomi Nakamura<sup>8</sup> , Tatsuji Nishizawa<sup>9</sup> , Atsushi Nakao<sup>2</sup> , Yasuo Ogawa<sup>10</sup> , Tatsu Kuwatani<sup>2</sup> , Kenji Nagata<sup>11</sup> , Tomomi Okada<sup>5</sup> , and Eiichi Takahashi<sup>12</sup> 

<sup>1</sup>Earthquake Research Institute, The University of Tokyo, Tokyo, Japan, <sup>2</sup>Research Institute for Marine Geodynamics, Japan Agency for the Marine-Earth Science and Technology (JAMSTEC), Yokosuka, Japan, <sup>3</sup>Department of Earth Resource Science, Akita University, Akita, Japan, <sup>4</sup>Research Center for Functional Materials, National Institute for Materials Science (NIMS), Tsukuba, Japan, <sup>5</sup>Research Center for Prediction of Earthquakes and Volcanic Eruptions, Tohoku University, Sendai, Japan, <sup>6</sup>Department of Earth System Science, University of Toyama, Toyama, Japan, <sup>7</sup>Department of Earth Science, Tohoku University, Sendai, Japan, <sup>8</sup>Research Institute of Earthquake and Volcano Geology, National Institute of Advanced Industrial Science and Technology (AIST), Tsukuba, Japan, <sup>9</sup>Mount Fuji Research Institute, Yamanashi Prefectural Government, Fujiyoshida, Japan, <sup>10</sup>Volcanic Fluid Research Center, Tokyo Institute of Technology, Tokyo, Japan, <sup>11</sup>Research and Services Division of Materials Data and Integrated System, National Institute for Materials Science (NIMS), Tsukuba, Japan, <sup>12</sup>Guangzhou Institute of Geochemistry, Chinese Academy of Sciences, Guangzhou, China

**Abstract** This study presents a forward model to quantify the P-wave velocity ( $V_p$ ), S-wave velocity ( $V_s$ ), and electrical conductivity ( $\sigma$ ) of the solid-liquid mixtures for a given set of pressure, temperature, lithology, liquid phase (aqueous fluid or melt), liquid fraction, and geometrical parameters in relation to the aspect ratio and connectivity of the liquid phase. This is based on previous experimental and theoretical studies on seismic velocity and electrical conductivity of solid rocks and liquid phases. A total of 78 lithologies, an aqueous fluid with NaCl (~0–10 wt.%), and mafic to felsic melt appropriate for the crust and the uppermost mantle conditions were described in terms of  $V_p$ ,  $V_s$ , and  $\sigma$ , as per previous experimental measurements and molecular dynamics simulation. This forward model is provided as a Windows executable program, and generates synthetic  $V_p$ ,  $V_s$ , and  $\sigma$ , referring to the seismic velocities and electrical conductivity observed in the northeast Japan arc. After generation of the synthetic  $V_p$ ,  $V_s$ , and  $\sigma$ , the original lithology and liquid parameters (phase, fraction, aspect ratio, and connectivity) were searched by implementing the grid search algorithm to map the misfit over the broad parameter space. The mapping shows the presence of a global misfit minimum around the optimized solution and the possibility of resolving the lithology and the liquid phase parameters based on the observed  $V_p$ ,  $V_s$ , and  $\sigma$  by using the forward model presented in this study.

**Plain Language Summary** Liquid phases such as aqueous fluid and magma present within the solid Earth play crucial roles in various geodynamic processes including earthquake and volcanic eruption, as well as in the evolution of our planet. This study aims to improve the subsurface imaging of the potentially variable types of liquid phase and solid rock, based on the near-surface observations concerning seismic velocity and electrical conductivity of the Earth's interior. We constructed a quantitative model to predict the physical properties of liquids and rocks. Then we used the model to perform "inversion," which estimates the physical properties of liquid and rock based on the observed seismic velocity and electrical conductivity. The inversion test using synthetic data shows the utility of our model.

## 1. Introduction

Aqueous fluids and melts in the Earth's crust and upper mantle (hereafter referred to as geofluids) play crucial roles not only in the hydrothermal and magmatic processes but also in various geodynamic processes and the Earth's evolution. For instance, aqueous fluids are presumed to reduce frictional strength

to induce earthquakes within the crust and along the plate boundary in NE Japan (Hasegawa et al., 2012; Sibson, 2009). Such fluids present at depth may chemically react with the rocks and reduce rock viscosity or form hydrous minerals and act as a lubricant in case they develop along the subducting slab. Thus, this enhances plate motion and subduction (Nakao et al., 2016; Seno & Kirby, 2014). A small amount of melt may exist at the bottom of the plates, which may also act as a lubricant at the lithosphere–asthenosphere boundary (Kawakatsu et al., 2009) and affect plate motion. Geofluids are also key in accounting for geochemical differentiation of the solid Earth's system, including large-scale heterogeneity represented by mantle geochemical hemispheres (Iwamori & Nakamura, 2015) because they act as effective transport agents of volatile and incompatible elements.

In this context, various studies attempted to resolve distribution of the geofluids in the Earth's interior, based on seismic and magnetotelluric (MT) structures and phenomena. In particular, low seismic velocity and/or high electrical conductivity ( $\sigma$ ) have been frequently highlighted to indicate the presence of fluids (e.g., Eberhart-Phillips et al., 1995), which is also examined through variations in the P-wave/S-wave velocity ratio ( $V_p/V_s$ ), seismic reflection, and attenuation (e.g., Nakajima et al., 2013; Okada et al., 2014). This can potentially be used to constrain the fluid parameters, including the fluid fraction, composition of the fluid phase (aqueous fluid or melt), and geometry of the fluid distribution (e.g., vein or grain boundary network) (Takei, 2002).

Imaging of subsurface fluid is a longstanding geophysical research, and industrial techniques to discover the oil–gas reservoir implement advanced quantification of the fluid parameters by combining various observations and experimental data. This includes physical well logging and precise physical properties for specific lithologies, such as typical reservoir sandstones (e.g., Carcione et al., 2007). For geoscientific research targeting greater depths where little or no drilling is possible, surface-based geophysical methods are the only means to resolve in situ distribution of geofluids within variable geological units of different lithologies and their bulk physical properties. In this case, a combination of seismic and MT methods is required to distinguish lithologies and geofluids including magma based on the different elastic and electrical properties, referred to as “joint inversion” (e.g., Moorkamp, 2017, and the references therein). Such surveys have been made in both oceanic and continental regions, including the Mantle Electromagnetic and Tomography “MELT” Experiment along the East Pacific Rise (The MELT Seismic Team, 1998), “Lithoprobe” (Hammer et al., 2011), and “USArray” (Long et al., 2014). Although the obtained seismic and electrical conductivity structures were not quantitatively combined, these large-scale surveys have provided new insights into the suboceanic and subcontinental structures: e.g., the discovery of an asymmetric melt distribution beneath the mid-ocean ridge and relict subducted or delaminated structures within the cratonic lithosphere.

The combined seismic and electrical conductivity approach would also be useful in subduction zone settings, where fluid flux from the subducting slab and melt generation occur in the mantle–crust system that consists of diverse lithologies over a wide range of pressure and temperature (Figures 1a and 1b). The seismic and electrical conductivity structures of subarc slab–mantle–crust systems have been extensively investigated in many subduction zones. For instance, in the northeastern Japan arc, a series of subduction zone processes, including water transport associated with the subducting slab, slab dehydration, mantle melting, and crustal seismicity, have been discussed based on various seismic and electrical conductivity studies (e.g., Ichiki et al., 2015; Kawakatsu & Watada, 2007; Kita et al., 2006; Nakajima et al., 2005; Ogawa et al., 2014), which have been compared with numerical models (e.g., Horiuchi & Iwamori, 2016; Iwamori, 1998). Figures 1c and 1d exhibit the results of seismic and electrical conductivity (resistivity) tomography along an across-arc section from a forearc to a volcanic zone (Okada et al., 2014; Ogawa et al., 2014). A significant range in electrical resistivity ( $1\text{--}10^4$  m/S) and S-wave velocity ( $\pm 6\%$ ) was observed with the vertically extending zone of low resistivity and velocity beneath the Naruko volcano, which suggests the presence of aqueous fluid and/or magma supplied to the volcano. However, these seismic and electrical conductivity observations have not been merged quantitatively to evaluate the physical properties of the rock–fluid or magma mixture.

This study aims to improve the subsurface imaging of potentially variable lithologies with geofluids by combining the quantitative estimates of seismic velocity and electrical conductivity, based on the existing experimental/theoretical knowledge of the physical properties of fluids, solids, and their mixtures. First, the physical properties of rocks and liquid phases (aqueous fluid and silicate melt) are described based on

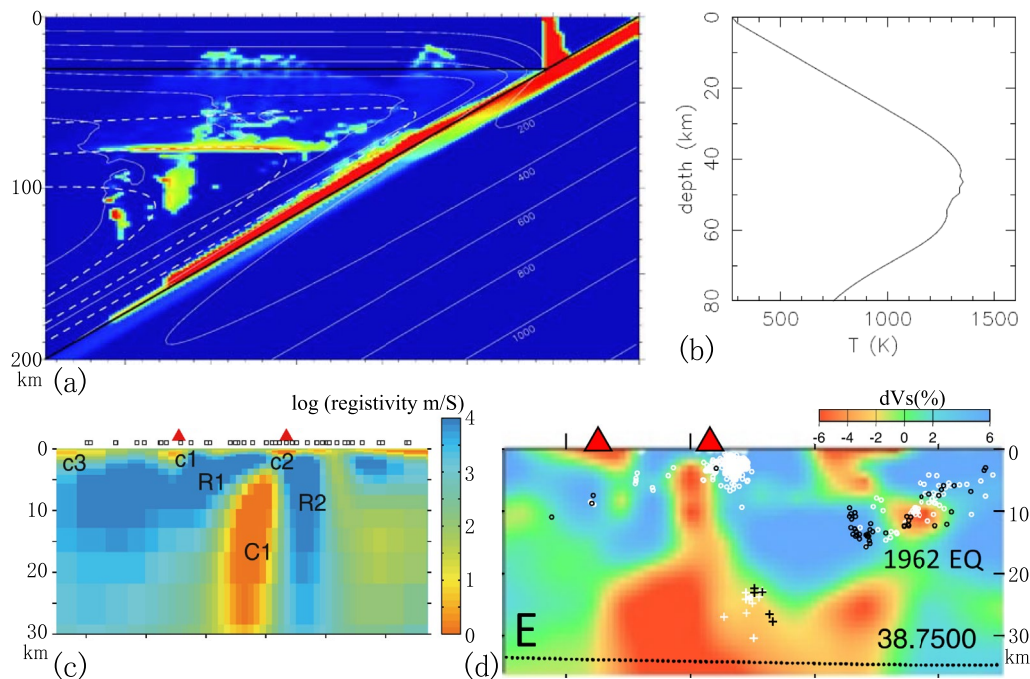


**Figure 1.** (a) Numerical simulation for thermal and fluid transport beneath the northeast (NE) Japan arc (Iwamori, 2007), where the color coding represents the  $\text{H}_2\text{O}$  concentration (0 wt.% [dark blue] to more than 6 wt.% [red]). The solid and broken lines represent the isothermal contour and the streamline in the  $350 \times 200$  km two-dimensional section, with the subducting Pacific Plate in the right-bottom half. (b) The temperature variation with depth near the volcanic front (beneath which the slab surface is at 80 km depth). Panels (c and d) are the across-arc structures at  $\sim 38.75^\circ\text{N}$  down to  $\sim 30$  km depth in terms of electrical resistivity from 0 to  $\sim 3.5$  m/S in log unit (Ogawa et al., 2014) and S-wave seismic velocity from  $dV_s = -6\%$  to  $6\%$  (Okada et al., 2014), including the Naruko Volcano (the right red triangle). Panels (c and d) are scaled to broadly match the depth scale.

previous experimental and theoretical studies, which are used to estimate the bulk properties as a mixture of these phases for a given set of pressure, temperature, lithology, liquid fraction, and geometry. We term this as “forward model,” and it can be utilized for the “inversion model,” which estimates the parameter values for lithology and liquid based on the observed seismic velocity and electrical conductivity.

## 2. Model

In this section, the physical properties of a mixture consisting of a solid rock and a liquid phase (aqueous fluid or melt) are described based on previous studies. For this purpose, the seismic velocities of the P-wave and S-wave ( $V_p$  and  $V_s$ , respectively) and electrical conductivity ( $\sigma$ ) of various lithologies and aqueous fluid/melt were compiled based on the experimental results and theoretical model predictions as a function of pressure and temperature. Second, on the basis of these single-phase properties,  $V_p$ ,  $V_s$ , and  $\sigma$  of the rock-fluid/melt mixture are modeled based on experimental and theoretical studies.

### 2.1. Rock Property

Seismic wave velocities are the primary source for revealing the structure of the Earth's interior, for which  $V_p$  and  $V_s$  have been measured for various crustal and upper mantle rocks (e.g., Christensen & Fountain, 1975; Kern, 1982; Kern & Tubia, 1993; Nishimoto et al., 2008). To describe  $V_p$  and  $V_s$  over a range of pressure ( $P$ ) and temperature ( $T$ ) within the Earth's crust and uppermost mantle, the following formulae were applied. The parameters used were determined based on the experimental measurements listed in Table 1. In total, 78 sets of  $V_p$  and  $V_s$  are provided for various rocks, which can be classified into 20 rock suites: quartzite (qtz), sedimentary sandstone and mudstone/shale (sed), limestone (lim), marble (mr), migmatite (mgm), quartz-K feldspar bearing mylonite (myl), metapelite (pel), kinzigite (kzg), gneiss (gns), granodiorite (grd),

No.	Abbrev.	Rock_type	Lithology	Vp ( $P, T$ ) km/s and Vs ( $P, T$ ) km/s where $P$ (pressure in GPa) and $T$ (temperature in degree Celsius)								Data source & sample name	
				Vp = $Vp_0 + b_1P + c_1T^*$			Vs = $Vs_0 + b_2P + c_2T^*$			Remarks			
				$Vp_0$	$b_1$	$c_1$	$Vs_0$	$b_2$	$c_2$				
1	hHCsed	Sediment	Sandstone	5.260	4.000E-01	-1.120E-03	2.930E+00	2.000E-01	-4.200E-04	$T^* = T-27$	Hughes and Cross (1951) Caplen Dome sandstone		
2	h32qtz	Sediment	Quartz sandstone	5.240	0	0	3.139	0	0	Sonic_log_data	Miller and Stewart (1990) 32		
3	h34lim	Limestone	Pekisko limestone	6.278	0	0	3.271	0	0	Sonic_log_data	Miller and Stewart (1990) 34		
4	h35lim	limestone	Pekisko limestone	6.171	0	0	3.311	0	0	Sonic_log_data	Miller and Stewart (1990) 35		
5	h36lim	limestone	Pekisko limestone	6.347	0	0	3.302	0	0	Sonic_log_data	Miller and Stewart (1990) 36		
6	h37lim	limestone	Pekisko limestone	5.927	0	0	3.293	0	0	Sonic_log_data	Miller and Stewart (1990) 37		
7	h38lim	Limestone	Pekisko limestone	5.867	0	0	3.081	0	0	Sonic_log_data	Miller and Stewart (1990) 38		
8	h39lim	Limestone	Pekisko limestone	5.127	0	0	2.803	0	0	Sonic_log_data	Miller and Stewart (1990) 39		
9	h40lim	Limestone	Pekisko limestone	6.226	0	0	3.151	0	0	Sonic_log_data	Miller and Stewart (1990) 40		
10	h41lim	Limestone	Pekisko limestone	6.037	0	0	3.183	0	0	Sonic_log_data	Miller and Stewart (1990) 41		
11	h42lim	Limestone	Pekisko limestone	5.531	0	0	2.910	0	0	Sonic_log_data	Miller and Stewart (1990) 42		
12	h85sed	Sediment	Shunda carbonated shale	4.771	0	0	2.798	0	0	Sonic_log_data	Miller and Stewart (1990) 85		
13	h86sed	Sediment	Shunda carbonated shale	5.058	0	0	2.821	0	0	Sonic_log_data	Miller and Stewart (1990) 86		
14	h87sed	Sediment	Shunda carbonated shale	5.366	0	0	2.989	0	0	Sonic_log_data	Miller and Stewart (1990) 87		
15	h88sed	Sediment	Shunda carbonated shale	5.524	0	0	3.096	0	0	Sonic_log_data	Miller and Stewart (1990) 88		
16	h92sed	Sediment	Detrital dolomite sandstone	6.171	0	0	3.375	0	0	Sonic_log_data	Miller and Stewart (1990) 92		
17	M0Bqtz	Sediment	Quartz sandstone	5.028	0	0	2.933	0	0	Zero porosity estimate	Miller and Stewart (1990) quartz sandstone		
18	M0Plim	Limestone	Pekisko limestone	6.264	0	0	3.290	0	0	Zero porosity estimate	Miller and Stewart (1990) Pekisko limestone		

**Table 1**  
*Continued*

No.	Abbrev.	Rock_type	Lithology	Vp ( $P, T$ ) km/s and Vs ( $P, T$ ) km/s where $P$ (pressure in GPa) and $T$ (temperature in degree Celsius)								Data source & sample name
				Vp <sub>0</sub>	b <sub>1</sub>	c <sub>1</sub>	Vs <sub>0</sub>	b <sub>2</sub>	c <sub>2</sub>	Remarks		
19	M0Nsed	Sediment	Nordegg sandstone	5.651	0	0	3.339	0	0	Zero porosity estimate	Miller and Stewart (1990) Nordegg sandstone	
20	M0Ssed	Sediment	Shunda carbonated shale	5.755	0	0	3.182	0	0	Zero porosity estimate	Miller and Stewart (1990) Shunda carbonated shale	
21	M0Dsed	Sediment	Detrital dolomite sandstone	6.739	0	0	3.550	0	0	Zero porosity estimate	Miller and Stewart (1990) detrital dolomite sandstone	
22	22_myl	Mylonite	qz-K-fd mylonite	4.76	1.463	-3.3E-05	3.02	0.675	8.2E-05	T* = T	Kern and Tubia (1993) Tb-363	
23	32_amp	Amphibolite	Amphibolite xenolith	5.64	0.8313	-0.0001752	3.32	0.3058	-0.0001456	T* = T	Kern et al. (1999) D95-19	
24	56_gns	Gneiss	Magnetite-bearing gneiss	5.79	0.2798	-0.0001572	3.56	0.0338	-4.26E-05	T* = T	Kern et al. (1999) TC3	
25	49_qtz	Quartzite	Quartzite	5.84	0.3856	-0.0004564	3.89	0.1547	-0.0001303	T* = T	Kern et al. (1999) D95-9	
26	30_grn	Granite	Granite	5.86	0.3785	-0.0002885	3.51	0.108	-8.62E-05	T* = T	Kern et al. (1999) D95-13	
27	06_grn	Granite	Granite	5.891	0.529	-0.000267	3.613	0.251	-0.000134	T* = T	Kern and Schenk (1988) 54a	
28	04_gns	Gneiss	Granitic gneiss	5.902	0.416	-0.000197	3.448	0.171	-7.3E-05	T* = T	Kern and Schenk (1988) 33	
29	29_pel	Metapelite	Metapelite xenolith	5.94	0.7431	-0.0001749	3.4	0.2406	-0.0001589	T* = T	Kern et al. (1999) D95-12	
30	48_gns	Gneiss	Tonalitic gneiss	5.95	0.6158	-0.0002622	3.51	0.2634	-0.0001297	T* = T	Kern et al. (1999) D95-7	
31	43_gns	Gneiss	Tonalitic granulite gneiss	5.96	0.4326	-0.0003722	3.58	0.182	-0.0001975	T* = T	Kern et al. (1999) D95-39	
32	41_hyu	Eclogite	Retrograde eclogite	5.98	0.6636	-0.0007914	3.26	0.2412	-0.0006021	T* = T	Kern et al. (1999) D95-35	
33	34_gns	Gneiss	Mylonitic trondhjemite gneiss	5.98	0.4487	-0.000309	3.62	0.1518	-0.0001424	T* = T	Kern et al. (1999) D95-22	
34	31_gns	Gneiss	Tonalitic gneiss	6.02	0.4555	-0.0002672	3.47	0.1561	-0.0001459	T* = T	Kern et al. (1999) D95-16	
35	53_grl	Granulite	Intermediate granulite	6.02	0.3811	-0.0004369	3.57	0.1038	-0.0002433	T* = T	Kern et al. (1999) HT1	
36	23_mgm	Migmatite	Nebulitic migmatite	6.05	0.428	-0.000505	3.54	0.155	-0.000141	T* = T	Kern and Tubia (1993) Tb-12	
37	03_grd	Granodiorite	Granodiorite	6.05	0.314	-0.000526	3.56	0.095	-0.000206	T* = T	Kern et al. (1993) 61-711	
38	05_grn	Granite	Granite	6.06	0.196	-0.000361	3.674	0.0237	-0.000141	T* = T	Kern and Schenk (1988) 44b	
39	14_kzg	Kinzigite	Kinzigite	6.09	0.473	-0.000723	3.66	0.118	-0.000289	T* = T	Kern and Tubia (1993) Tb-Kz	

**Table 1**  
*Continued*

Vp ( $P, T$ ) km/s and Vs ( $P, T$ ) km/s where $P$ (pressure in GPa) and $T$ (temperature in degree Celsius)											
No.	Abbrev.	Rock_type	Lithology	Vp = $Vp_0 + b_1 P + c_1 T^*$			Vs = $Vs_0 + b_2 P + c_2 T^*$			Remarks	Data source & sample name
				$Vp_0$	$b_1$	$c_1$	$Vs_0$	$b_2$	$c_2$		
40	08_ton	Tonalite	Tonalite	6.095	0.442	-0.000253	3.616	0.128	-2.1E-05	$T^* = T$	Kern and Schenk (1988) 35a
41	46_gns	Gneiss	Trondhjemitic gneiss	6.11	0.4307	-0.0003913	3.62	0.2283	-0.0002824	$T^* = T$	Kern et al. (1999) D95-44
42	15_hyu	Hydrated ultramafic rock	Serpentinized peridotite	6.23	0.394	-0.000821	3.24	0.062	-0.000428	$T^* = T$	Kern and Tubia (1993) Tb-580
43	54_gns	Gneiss	Tonalitic gneiss	6.23	0.3585	-0.0003123	3.67	0.1069	-0.0001606	$T^* = T$	Kern et al. (1999) HT4
44	17_hyu	Lherzolite	Lherzolite	6.27	0.39	-0.000988	3.38	0.071	-0.000487	$T^* = T$	Kern and Tubia (1993) Tb-490
45	07_grd	Granodiorite	Granodiorite	6.272	0.202	-0.000382	3.609	0.061	-4.1E-05	$T^* = T$	Kern and Schenk (1988) 45b
46	27_gns	Gneiss	Tonalitic gneiss	6.28	0.3516	-0.0002688	3.56	0.1113	-0.0001952	$T^* = T$	Kern et al. (1999) D95-10
47	47_pel	Metapelite	Metapelite	6.29	0.2983	-0.0002979	3.52	0.0956	-0.0002509	$T^* = T$	Kern et al. (1999) D95-6
48	28_gbr	Gabbro	Gabbro xenolith	6.38	0.4422	-0.0002281	3.67	0.1494	-0.0001928	$T^* = T$	Kern et al. (1999) D95-11
49	52_grl	Granulite	Mafic granulite	6.39	0.5483	-0.0001681	3.69	0.1814	-0.0001026	$T^* = T$	Kern et al. (1999) HL9
50	55_amp	Amphibolite	Amphibolite	6.50	0.5686	-0.0002255	3.76	0.199	-0.0001925	$T^* = T$	Kern et al. (1999) HT6
51	24_myl	Mylonite	qz-K-fd mylonite	6.52	0.437	-0.000488	3.76	0.137	-0.000182	$T^* = T$	Kern and Tubia (1993) Tb-Lvi
52	18_hyu	Peridotite	Dunite	6.55	0.436	-0.00089	3.58	0.093	-0.000412	$T^* = T$	Kern and Tubia (1993) Tb-491
53	51_grl	Granulite	Mafic granulite	6.65	0.4167	-0.00023	3.82	0.1032	-0.0001486	$T^* = T$	Kern et al. (1999) HL3
54	33_gbr	Gabbro	Metagabbro	6.67	0.4148	-0.0002239	3.9	0.1409	-0.0001636	$T^* = T$	Kern et al. (1999) D95-2
55	44_gbr	Gabbro	Metagabbro	6.76	0.3456	-0.0002717	3.88	0.1165	-0.0002036	$T^* = T$	Kern et al. (1999) D95-4
56	50_mrb	Marble	Marble	6.79	0.5796	-0.0004751	3.76	0.1677	-0.000417	$T^* = T$	Kern et al. (1999) FH7
57	37_ecl	Eclogite	Eclogite	6.84	0.5308	-0.0002752	3.90	0.1229	-0.0002693	$T^* = T$	Kern et al. (1999) D95-26
58	25_ecl	Eclogite	Eclogite (mylonitic)	6.98	0.407	-0.00036	3.97	0.162	-0.000211	$T^* = T$	Kern and Tubia (1993) Tb-26
59	38_lhr	Lherzolite	Garnet lherzolite	6.99	0.25	-0.0005823	3.87	0.0538	-0.0003853	$T^* = T$	Kern et al. (1999) D95-27
60	01_gbr	Gabbro	Gabbronorite	7.10	0.30	-0.00037	3.80	0.10	-0.00038	$T^* = T$	Kono et al. (2006) Kohistan gabbronorite
61	26_ecl	Eclogite	Retrogressed eclogite	7.10	0.18	-0.000312	3.98	0.058	-0.000187	$T^* = T$	Kern and Tubia (1993) Tb-590
62	21_gbr	Gabbro	Metagabbro	7.10	0.125	-0.000478	4.11	0.012	-0.000387	$T^* = T$	Kern and Tubia (1993) Tb-358
63	42_ecl	Eclogite	Eclogite	7.12	0.8614	-0.0003758	4.35	0.1409	-0.0002636	$T^* = T$	Kern et al. (1999) D95-38

**Table 1**  
*Continued*

Vp ( $P, T$ ) km/s and Vs ( $P, T$ ) km/s where $P$ (pressure in GPa) and $T$ (temperature in degree Celsius)											
No.	Abbrev.	Rock_type	Lithology	$Vp = Vp_0 + b_1 P + c_1 T^*$			$Vs = Vs_0 + b_2 P + c_2 T^*$			Remarks	Data source & sample name
				$Vp_0$	$b_1$	$c_1$	$Vs_0$	$b_2$	$c_2$		
64	10_amp	Amphibolite	Amphibolite	7.17	0.07	-0.0007	3.97	0.04	-0.0004	$T^* = T$	Nishimoto et al. (2008) 6982203
65	12_gbr	Gabbro	hb gabbro	7.24	0.14	-0.0008	4.05	0.06	-0.0005	$T^* = T$	Nishimoto et al. (2008) HG-08
66	11_amp	Amphibolite	px amphibolite	7.24	0.07	-0.0008	4.29	0.04	-0.0005	$T^* = T$	Nishimoto et al. (2008) HG-06
67	13_gbr	Gabbro	hb-px gabbro	7.24	0.15	-0.0006	4.29	0.07	-0.0005	$T^* = T$	Nishimoto et al. (2008) 6982204
68	39_gbr	Metagabbro	Metagabbro	7.25	0.2314	-0.0003662	4.18	0.0578	-0.0002662	$T^* = T$	Kern et al. (1999) D95-3
69	09_hbd	Amphibolite	Hornblendite	7.26	0.11	-0.0009	3.92	0.05	-0.0006	$T^* = T$	Nishimoto et al. (2008) 6982102
70	45_ecl	Eclogite	Eclogite	7.45	0.3723	-0.000418	4.54	0.1521	-0.0002709	$T^* = T$	Kern et al. (1999) D95-40
71	40_ecl	Eclogite	Eclogite	7.46	0.6089	-0.0003215	4.37	0.3173	-0.0001945	$T^* = T$	Kern et al. (1999) D95-32
72	02_lhr	Lherzolite	Spinel-garnet lherzolite	7.68	0.166	-0.000262	4.25	0.004	-8.4E-05	$T^* = T$	Kern et al. (2002) SL98-04
73	35_ecl	Eclogite	Eclogite	7.68	0.3799	-0.0003804	4.55	0.1758	-0.000258	$T^* = T$	Kern et al. (1999) D95-24
74	36_ecl	Eclogite	Eclogite	7.73	0.5439	-0.0003118	4.62	0.222	-0.0002165	$T^* = T$	Kern et al. (1999) D95-25
75	16_lhr	Lherzolite	Lherzolite	8.06	0.273	-0.000494	4.67	0.105	-0.000294	$T^* = T$	Kern and Tubia (1993) Tb-724
76	20_hrz	Harzburgite	Harzburgite	8.09	0.16	-0.000621	4.73	0.033	-0.000391	$T^* = T$	Kern and Tubia (1993) Tb-357-3
77	19_hrz	Harzburgite	Harzburgite	8.10	0.13	-0.000636	4.72	0.024	-0.000303	$T^* = T$	Kern and Tubia (1993) Tb-357-1
78	hKMprd	Peridotite	Garnet lherzolite	Calculated on P-T grid points for ol 59.8%, opx 21.1%, cpx 7.6%, gar 11.5%					$T^* = T$	Matsukage et al. (2005)	

Note.  $T^*$  is used to calculate Vp and Vs (as in the top of Table 1), which is related to the actual temperature T. In one sample,  $T^* = T - 27$ .

granulite (grl), granite (grn), tonalite (ton), hornblendite (hbd), amphibolite (amp), gabbro (gbr), eclogite (ecl), harzburgite (hrz), serpentinized-hydrated ultramafic rock (hyu), and lherzolite (lhr).

Experiments at relatively high pressures ( $P$ ) and temperatures ( $T$ ) have been conducted for various types of igneous, metamorphic, and ultramafic rocks to reproduce the mid/lower crust to the uppermost mantle conditions with a linear function of  $P$  and  $T$  for the individual rocks (e.g., Kern & Schenk, 1988; Kern & Tubaia, 1993; Kern et al., 1993, 1999, 2001, 2002; Kono et al., 2006; Punturo et al., 2005; D. Wang et al., 2005). On the other hand, velocity measurements on sedimentary rocks collected from wells have also been conducted (e.g., Miller & Stewart, 1990), which report both the velocities as a function of porosity, including the estimated porosity-free velocity. Even for high-pressure experiments, a velocity reduction due to the presence of cracks is recognized at relatively low pressures (e.g., <300–400 MPa). Most of the previous works listed above express the  $V_p$  and  $V_s$  with a linear formulation based on relatively high pressures. In addition, mineralogical data and Voigt-Reuss-Hill average of the ultramafic rocks were also utilized for the constituent minerals and modal compositions to calculate  $V_p$  and  $V_s$  for peridotite (Matsukage et al., 2005).

These previously reported velocities are listed in Table 1 and were incorporated in the present study. Figure 2 exhibits the reproduced  $V_p$  and  $V_s$  from 0 to 2 GPa and 0–1,200°C (273–1,473 K) for gabbro (lower plane) and peridotite (upper plane), respectively. The velocities of peridotite exhibit a greater temperature dependence and a smaller pressure dependence than those of gabbro, as expressed by the slope of the plane. Due to this difference, the variations in  $V_p$  and  $V_s$  along the geotherm shown in Figure 1b are distinct; the velocities of peridotite (green line in Figure 2) decrease from 0 to ~1.2 GPa and then increase slightly to 2.0 GPa, whereas for gabbro (red line in Figure 2),  $V_p$  monotonously increases and  $V_s$  shows a slight decrease from 0 to ~1 GPa and an increase to 2 GPa. Figure 2 also displays the  $V_p$  and  $V_s$  of several other rock types along the geotherm, and different individual behaviors are observed. It is noted that the  $P$ - $T$  condition may exceed the solidus along the geotherm for several lithologies, particularly under hydrous conditions, and such effects on the physical properties of partially molten rock will be discussed separately.

Figure S1 shows  $V_p$  and  $V_s$  of the rocks in Table 1 as a function of pressure for the selected temperatures, which confirms the different behaviors. The experimental data reported by Punturo et al. (2005) and D. Wang et al. (2005), which are not listed in Table 1, are plotted in Figure S1 to examine how the data can be reproduced using the formulae of similar rock types in Table 1. The fit is reasonably good and indicates the applicability of the  $P$ - $T$ - $V_p$ - $V_s$  relationship to a wide range of crustal and upper mantle conditions.

The electrical conductivity measurements are not available for all 20 individual rock suites, but they can be broadly represented by fewer rock types based on the constituent minerals (Figure 3 and Table 2). Although the factors that control the electrical conductivity of polycrystalline rocks is not fully understood, including the effects of grain boundaries, accessory phases, and rock texture (Fuji-ta et al., 2007; Stesky & Brace, 1973; ten Grotenhuis et al., 2005), Figure 3 indicates that the electrical conductivity and its temperature dependence (i.e., activation energy) differ systematically depending on the rock suites. Fuji-ta et al. (2007) reported the electrical conductivity of the Higo gneiss from southern Japan, composed mainly of quartz, plagioclase, K-feldspar, and a subordinate amount of mafic minerals (including biotite and garnet) (Kobayashi et al., 2005), which can be regarded as an intact material that represents upper crustal lithologies. In this study, we utilize the experimental result of Fuji-ta et al. (2007), as a function of temperature using the Arrhenius equation (Line 1 in Figure 3) for gneiss (gns), granite (grn), kinzigite (kzg), migmatite (mgm), mylonite (myl), metapelite (pel), quartzite (qtz), and sediments (sed).

For lithologies representing felsic to intermediate composition of granodiorite (grd), granulite (grn), and tonalite (ton), we applied the experimental results of Fuji-ta et al. (2004) for the Hidaka granulite (Line 2 in Figure 3), which is predominantly composed of plagioclase, K-feldspar, quartz, garnet, cordierite, and biotite (Osanai, 1985). Similarly, the electrical conductivities of the mafic crustal rocks, amphibolite (amp), gabbro (gbr), and hornblendite (hbd), are represented by the experimental results of the Higo metamorphic mafic rocks of amphibolite–granulite facies, mainly consisting of plagioclase, amphibole, and garnet (Line 3 in Figure 3, after Fuji-ta et al., 2011). Equations and parameters based on experimental results for natural antigorite samples by Reynard et al. (2011) were used to calculate the electrical conductivity of serpentinite (hydrous ultramafic rock, hyu, Line 5 in Figure 3). The electrical conductivity model of ultramafic rocks provided by D. Wang et al. (2008), which is a function of bulk water content and bulk Mg# ( $Mg/[Mg + Fe]$ ),

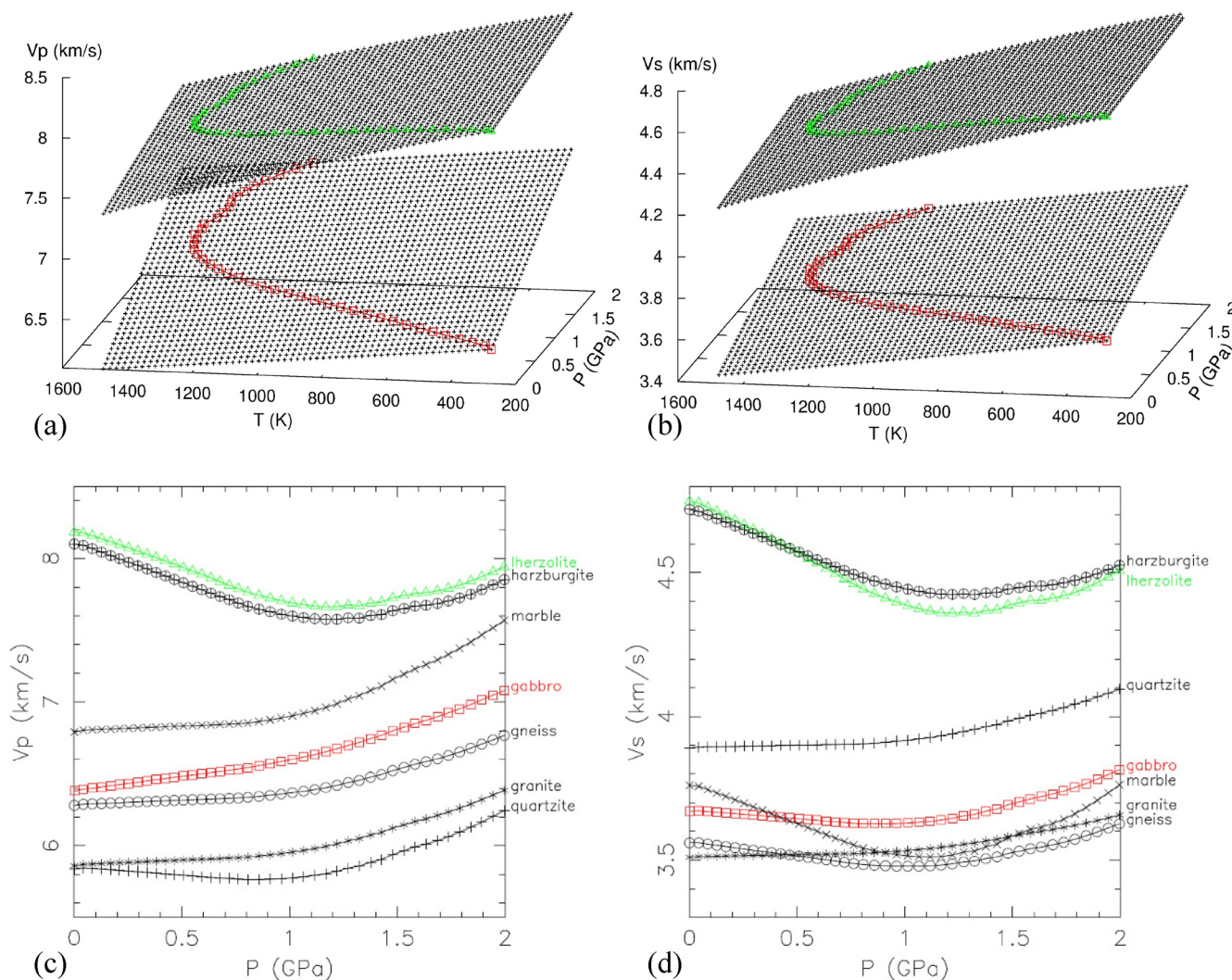


**Figure 2.** The upper row shows the 3D diagrams (a and b) for calculated  $V_p$  and  $V_s$  from 0 to 2 GPa and 0–1,200°C (273–1,473 K) for gabbro (lower plane for no. 48 “28\_gbr” in Table 1) and lherzolite (upper plane for no. 78 “hKMprd” in Table 1). The green and red lines represent the  $P-T-V$  variations along the geotherm (Figure 1b) for peridotite and gabbro, respectively. The lower row (c and d) shows the pressure versus  $V_p$  and  $V_s$  from 0 to 2 GPa along the geotherm for seven different lithologies from Table 1 (lherzolite “hKMprd,” quartzite “49\_qtz,” granite “30\_grn,” gneiss “27\_gns,” gabbro “28\_gbr,” marble “50\_mbr,” and harzburgite “19\_hrz”).

was used to calculate the electrical conductivity of eclogite (ecl), lherzolite (lhr), and harzburgite (hrz) (Lines 4, 6, and 7 in Figure 3). The electrical conductivity of eclogite (Line 4 in Figure 3) was calculated assuming Mg# = 0.6, which broadly reproduced the experimental results for eclogite (Dai et al., 2016). For lherzolite and harzburgite, we used Mg# = 0.900 and 0.923, respectively, as given in the equation of D. Wang et al. (2008). The water content was fixed to the experimental value used by D. Wang et al. (2008) (i.e., 0.0126 wt.% for lherzolite and 0.0131 wt.% for harzburgite and eclogite).

For the pressure and temperature range within the crust and uppermost mantle (e.g., Figure 1), most of the above-mentioned experimental results can be approximated by a linear function in the  $1/T$  versus  $\log \sigma$  space without a significant pressure effect. However, it is noted that the temperature dependence is large and a small uncertainty in activation energy may lead to large variations in  $\sigma$ . It is also noted that, at higher temperatures (e.g.,  $>1,250$  K and  $1,000/T < 0.8$ ), different conduction mechanisms may operate with steeper slopes (e.g., Dai et al., 2018; Yoshino & Katsura, 2013; Yoshino et al., 2009). For the electrical conductivity of calcite, several phase changes occur at different temperatures, of which the phase change between calcite IV and V exhibits different electrical conductivity slopes at  $\sim 1,250$  K (Mirwald, 1979). Although a

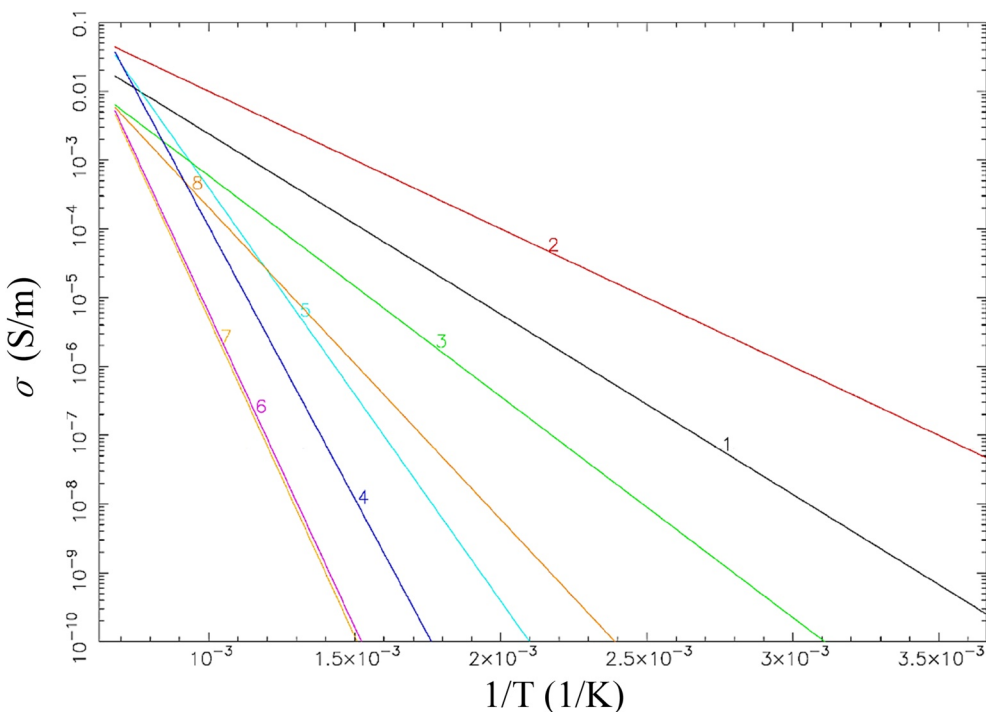


**Figure 3.** Electrical conductivity of eight rock suites used in the study. The line numbers and the corresponding rock types are listed in Table 2.

significant scatter would occur below  $\sim 750$  K (Mirwald, 1979), a linear relationship may account for the experimental data (Wada et al., 2012), as indicated by Line 8 in Figure 3.

## 2.2. Aqueous Fluid Property

The nature and composition of aqueous fluids in the Earth's crust and upper mantle, particularly beneath arcs and subduction zones, have been studied via high-pressure experiments (e.g., Brenan et al., 1995; Keppler, 1996; Kessel et al., 2005), incorporating geochemical constraints on arc magmas and deep-seated spring waters (e.g., Kusuda et al., 2014; Nakamura et al., 2008; Pearce et al., 2005), and fluid inclusions in mantle-derived xenoliths (e.g., Ionov, 2010; Ishimaru & Arai, 2008; Kawamoto et al., 2013). These studies have revealed that the aqueous fluids contain appreciable and variable amounts of NaCl. In addition, some of them are highly saline, such as the Arima-type spring waters that contain NaCl which is  $\sim 2.5$  times higher than seawater (Kusuda et al., 2014). Sakuma and Ichiki (2016a, 2016b) proposed a comprehensive model to describe the physical properties (density, isothermal compressibility, and electrical conductivity) of such aqueous fluids, based on both molecular dynamics (MD) simulation and experiments (Bannard, 1975; Driesner, 2007; Wagner & Prüß, 2002).

In this study, we used the parameterized results of Sakuma and Ichiki (2016a, 2016b), which enabled us to describe the physical properties as a function of pressure, temperature, and NaCl concentration of the fluid up to 2.0 GPa, 2,000 K, and 10 wt.% NaCl, respectively. Figure 4 shows examples of P-wave velocity, density, and electrical conductivity in the pressure–temperature space for an aqueous fluid with 5 wt.% NaCl (that corresponds to the natural Arima-type brine [Kusuda et al., 2014] and the fluid inclusions in mantle xenoliths [Kawamoto et al., 2013]). The ranges of  $V_p$  and  $\sigma$  of the aqueous fluid along the model geotherm are much lower and higher, respectively, than those of any lithology shown in Figures 2 and 3; for example, the electrical conductivity is greater than 1.0 S/m for the aqueous fluids (except for  $\sim 0$  wt.% NaCl fluid, Figure 4) and much less than 0.1 S/m for the rock suites (Figure 3).

There is a slight gap in electrical conductivity at 673 K as the MD simulations were performed at  $> 673$  K and the experimental data were used for the parameterization at  $< 673$  K. However, the gap was small compared

**Table 2**

Electrical Conductivity ( $\sigma$ ) of Rocks Used in This Study and the Data Sources

Rock type	Rock name	Line no.	$\sigma_0$	E	Conductivity models	Experimental detail: Sample	Experimental P	Experimental T
Felsic rock/ sedimentary rock	Gneiss (gns), granite (grn), kinzigite (kzg), migmatite (mgm), mylonite (myl), metapelite (pel), quartzite (qtz) and sediments (sed)	1	1.00E+00	5.02E+01	Optimized based on the data of Fuji-ta et al. (2007)	Gneiss dominantly composed of plagioclase, orthoclase, quartz, biotite, and garnet.	1 GPa	600–1,000
Felsic to intermediate rock	Granodiorite (grd), granulite (grn), and tonalite (ton)	2	1.00E+00	3.76E+01	Optimized based on the data of Fuji-ta et al. (2004)	Granulite composed of garnet, cordierite, biotite, quartz and plagioclase with minor pyrrhotite	1 GPa	300–900
Mafic rock	Amphibolite (amp), gabbro (gbr), and hornblendite (hbd)	3	9.56E−01	6.15E+01	Optimized based on the data of Fuji-ta et al. (2011)	Amphibolite mainly composed of amphibole, garnet, plagioclase, albite, and anorthite	0.5 GPa	~300–1,100
Limestone-marble	Limestone (lim), marble (mrh)	8	7.00E+00	8.68E+01	Mirwald (1979)	Calcite crystals	40 bar	573–1,473
Ultramafic rock	Hydrous ultramafic rock (hyu)	5	4.00E+02	1.15E+02	Reynard et al. (2011)	Three natural antigorite samples (high-pressure serpentinite from Cuba, Oeyama ultramafic body, and vein coexisting with dolomite, Nagahama, Ehime prefecture, Japan)	2.0–3.5 GPa	500–800
Eclogite (ecl)		4	8.68E+03	1.51E+02	D. Wang et al. (2008)	Natural dunite (Tibet, China), pyroxenite xenolith, and lherzolite xenolith (HeBei province, China)	2–3 GPa	1,273–1,573
Lherzolite (lhr)		6	8.46E+03	1.75E+02				
Harzburgite (hrz)		7	8.68E+03	1.77E+02				

Note.  $\sigma = \sigma_0 \exp(-E/kT)$  and  $\sigma_0$  is conductivity (S/m) at infinitely high temperatures, E is the activation energy (kJ/mol), T is absolute temperature, and k is the Boltzmann constant.

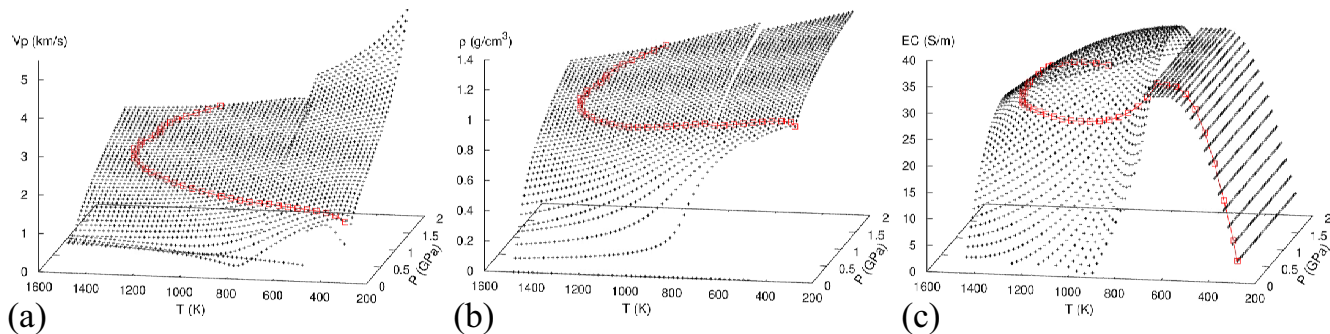


**Figure 4.** Physical properties of aqueous fluid with 5 wt.% NaCl for (a)  $V_p$ , (b) density ( $\rho$ ), and (c) electrical conductivity ( $\sigma$  [EC in the diagram]). The red line illustrates the properties along the geothermal gradient (Figure 1b) in a subduction zone. It is noted that at temperatures  $<673$  K, the experimental data nearly exhibits a constant electrical conductivity for pressures less than 0.4 GPa (Bannard, 1975; Quist & Marshall, 1968). Although the experimental pressure range is less than 0.4 GPa, the electrical conductivity extrapolated to the pressure higher than the experimental range is consistent with the MD simulation at 673 K and a recent experiment (Simmyo & Keppeler, 2017), and it is implemented in this study. At relatively low pressures and high temperatures (e.g.,  $<0.2$  GPa and  $>1,000$  K),  $\sigma$  is set to zero, where the extrapolated values of  $\sigma$  based on MD simulation becomes negative.

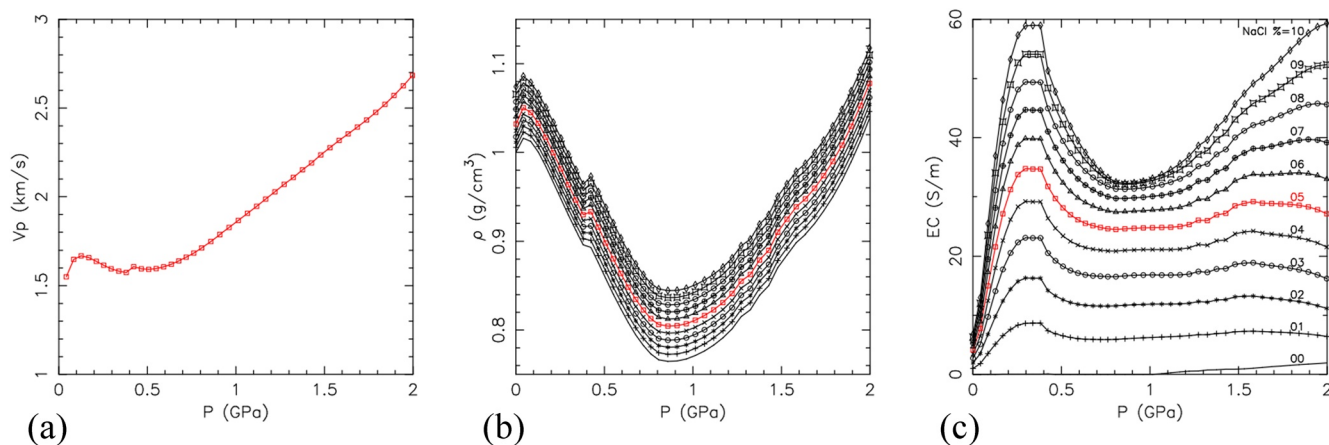


**Figure 5.** P-wave velocity ( $V_p$ ), density ( $\rho$ ), and electrical conductivity ( $\sigma$  [EC in the diagram]) of aqueous fluids with NaCl concentrations from  $\sim 0$  to 10 wt.%, along the geothermal gradient in Figure 1b, based on Sakuma and Ichiki (2016a, 2016b). The NaCl-dependence of  $V_p$  is small and only  $V_p$  with NaCl = 5 wt.% is shown for clarity of the figure.

to the overall range of electrical conductivity from  $\sim 0$  (for nearly pure water) to 70 S/m (10 wt.% NaCl) and in density from  $<0.2$  g/cm<sup>3</sup> (at relatively low pressure and high temperature, e.g.,  $<0.1$  GPa and  $>1,000$  K) to  $\sim 1.3$  g/cm<sup>3</sup> (at relatively high-pressure, low temperature, and high salinity, e.g.,  $>1$  GPa,  $<700$  K, and 10 wt.% NaCl). Rather, smooth variations in the physical properties with pressure along the geotherm (Figure 5) imply that the gap described above is small. For the entire NaCl contents, a maximum electrical conductivity is displayed from 0.3 to 0.4 GPa as pointed out by Sakuma and Ichiki (2016b). In addition, a minimum density is observed from 0.8 to 0.9 GPa.

### 2.3. Melt Property

The seismic velocities of silicate melts were estimated for a given set of pressure ( $P$ ), temperature ( $T$ ), major element composition, and H<sub>2</sub>O concentration, based on Ueki and Iwamori (2016). They optimized the molar volume ( $V$ ) and its pressure–temperature derivatives of the H<sub>2</sub>O end-member component in silicate melts, as well as the pressure derivative of bulk modulus. This is internally consistent with the parameter values for the volumetric properties of anhydrous silicate melt reported by Lange and Carmichael (1987, 1990) and consistently accounts for previously reported experimental results of ultramafic to felsic melts at pressures of 0–4.29 GPa. The elastic properties of dry-hydrous silicate melts were obtained based on the third-order Birch–Murnaghan equation of state. The Birch–Murnaghan equation, which was originally derived from finite strain theory for solid materials (Birch, 1947), has been widely applied to model the  $P$ – $V$  relations and phase equilibria of silicate melts (e.g., Ghiorso et al., 2002; Mosenfelder et al., 2009; Rigden et al., 1989; Stixrude & Bukowinski, 1990).

A basalt composition from the Iwate Volcano on the volcanic front of the NE Japan arc was used to calculate the elastic properties, including seismic velocity (Figure 6). The SiO<sub>2</sub> content of basalt was  $\sim 51$  wt.% (Ueki & Iwamori, 2016), and the H<sub>2</sub>O content was assumed to be 5 wt.%, based on the evaluated primary magma composition of the Iwate volcano (Kuritani et al., 2014). We calculated the P-wave velocity of hydrous basalt based on the density and isothermal bulk modulus ( $K_T$ ) of hydrous basalt, which is derived from the isothermal bulk modulus at 1 bar ( $K_{T0}$ ), molar volume at 1 bar ( $V_0$ ), and the pressure derivative of  $K_T$  ( $K'$ ), assuming linear mixing between an anhydrous melt and the H<sub>2</sub>O component in the melt. Murase and McBirney (1973) demonstrated that the difference between isothermal and isentropic bulk modulus ( $K_T$  and  $K_S$ ) is negligible in a silicate melt, and  $K_T$  was used to calculate the seismic velocity of hydrous basalt. The shear modulus of silicate melts is negligible, and the S-wave velocity is assumed to be zero (Rivers & Carmichael, 1987; Webb, 1992).

The electrical conductivity of melts is calculated using the numerical model SIGMELTS (Pommier & Le Trong, 2011). SIGMELTS is a software that aims to facilitate the modeling of the electrical properties of geological materials, particularly for melts including both silicate and carbonatite liquids. The model can

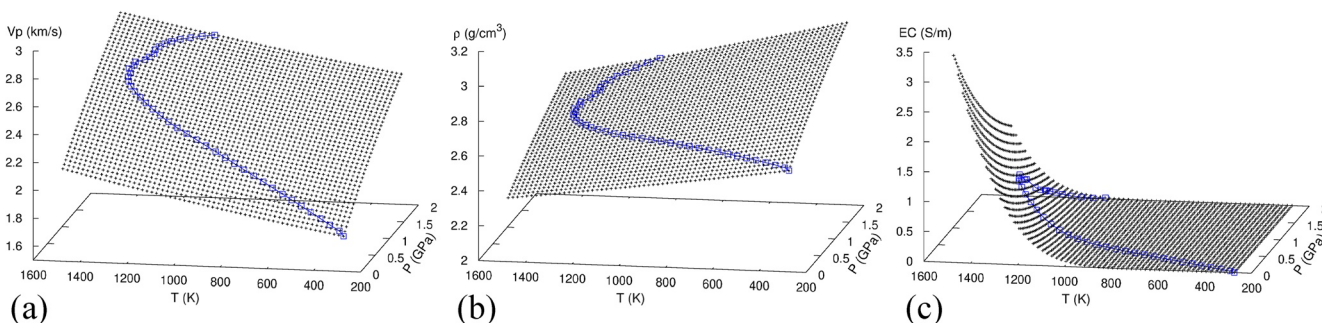


**Figure 6.** Physical properties of a basaltic melt (Iwate basalt, IW17,  $\text{SiO}_2 = 51.38 \text{ wt. \%}$ ,  $\text{Na}_2\text{O} = 1.91 \text{ wt.\%}$ , Ueki & Iwamori, 2016) for (a)  $V_p$ , (b) density ( $\rho$ ), and (c) electrical conductivity  $EC(=\sigma)$ . The blue line illustrates the properties along the geothermal gradient (Figure 1b) in a subduction zone setting.

be used to calculate the electrical conductivities of various dry and hydrous silicate melts (40–80  $\text{SiO}_2$  wt.%) at temperatures between 1,073–1,673 K and pressures up to 2.5 GPa (Pommier et al., 2008). In SIGMELTS, which was modified after the semiempirical model of Pommier et al. (2008), the electrical conductivity of silicate melt is modeled as a function of  $T$ ,  $P$ ,  $\text{SiO}_2$ ,  $\text{Na}_2\text{O}$ , and  $\text{H}_2\text{O}$  concentrations based on the Arrhenius equation. The parameters were optimized based on the experimentally determined conductivities of dry and hydrous melts at various temperatures and pressures (Pommier et al., 2008). An example for the Iwate basalt (the diagram for EC in Figure 6c) shows that the electrical conductivity depends on both  $P$  (0–2 GPa) and  $T$  (the effective range from 1,073 to 1,673 K) with a greater variation for the temperature within the plot range.

These models for seismic velocity and electrical conductivity are also applicable from andesitic to felsic melt, as well as basaltic melt (Figure 7). The top row (Figures 7a–7c) represents the variations in  $V_p$ – $\rho$ – $EC(=\sigma)$  along the geotherm, as shown in Figure 1b. Both  $V_p$  and  $\rho$  decrease from basaltic to granitic melt, and from 0.1 wt.% to 5.0 wt.%  $\text{H}_2\text{O}$ , whereas  $EC(=\sigma)$  exhibits a similar value along the same geotherm, rather insensitive to the melt composition. The second row in Figure 7 (7d–7f) shows  $V_p$ – $\rho$ – $EC$  of the basaltic melt, andesitic melt, and felsic melt at 1,200°C (1,473 K), 1,000°C (1,273 K), and 800°C (1,073 K), respectively. Here,  $V_p$  and  $\rho$  exhibits variations of a similar magnitude to those in Figures 7a and 7b, indicating a strong compositional dependence. Compared to Figure 7c, the electrical conductivity in Figure 7f exhibits greater differences among the three types of melt at different temperatures, which confirms that temperature is the primary factor controlling the  $EC$  of the melt.

#### 2.4. Properties of Solid-Liquid Mixture

The elastic and electrical properties of solid-liquid (aqueous fluid or melt) mixtures are important for evaluating the presence and volume of aqueous fluids or melts in the Earth based on the observed seismic velocity and electrical conductivity. For the elastic properties of mixture, various models have been proposed depending on the geometrical configuration of solid-liquid, such as spheroidal models (e.g., Wu, 1966), crack models (Kachanov et al., 1994; O'Connell & Budiansky, 1974) and a tube model (Mavko, 1980). In this study, the seismic velocities of solid-liquid mixture systems were calculated after Takei (2002), who integrated these various models by relating them to the oblate spheroid model in terms of the “equivalent aspect ratio.” Consequently, the model of Takei (2002) is applicable to a wide range of equilibrium-disequilibrium geometries, which may represent various conditions in the crust and uppermost mantle with variable pressure and temperature. Takei (2002, 2005) presented a set of linearized equations to express the P-wave and S-wave velocity variations ( $\Delta V_p$  and  $\Delta V_s$ ) as follows:

$$\frac{\Delta V_p}{V_p^0} = \left[ \frac{\frac{(\beta - 1)\Lambda_{K_b}}{(\beta - 1) + \Lambda_{K_b}} + \frac{4}{3}\gamma\Lambda_N}{1 + \frac{4}{3}\gamma} - \left(1 - \frac{\rho_L}{\rho_S}\right) \right] \frac{\phi}{2} \quad (1)$$

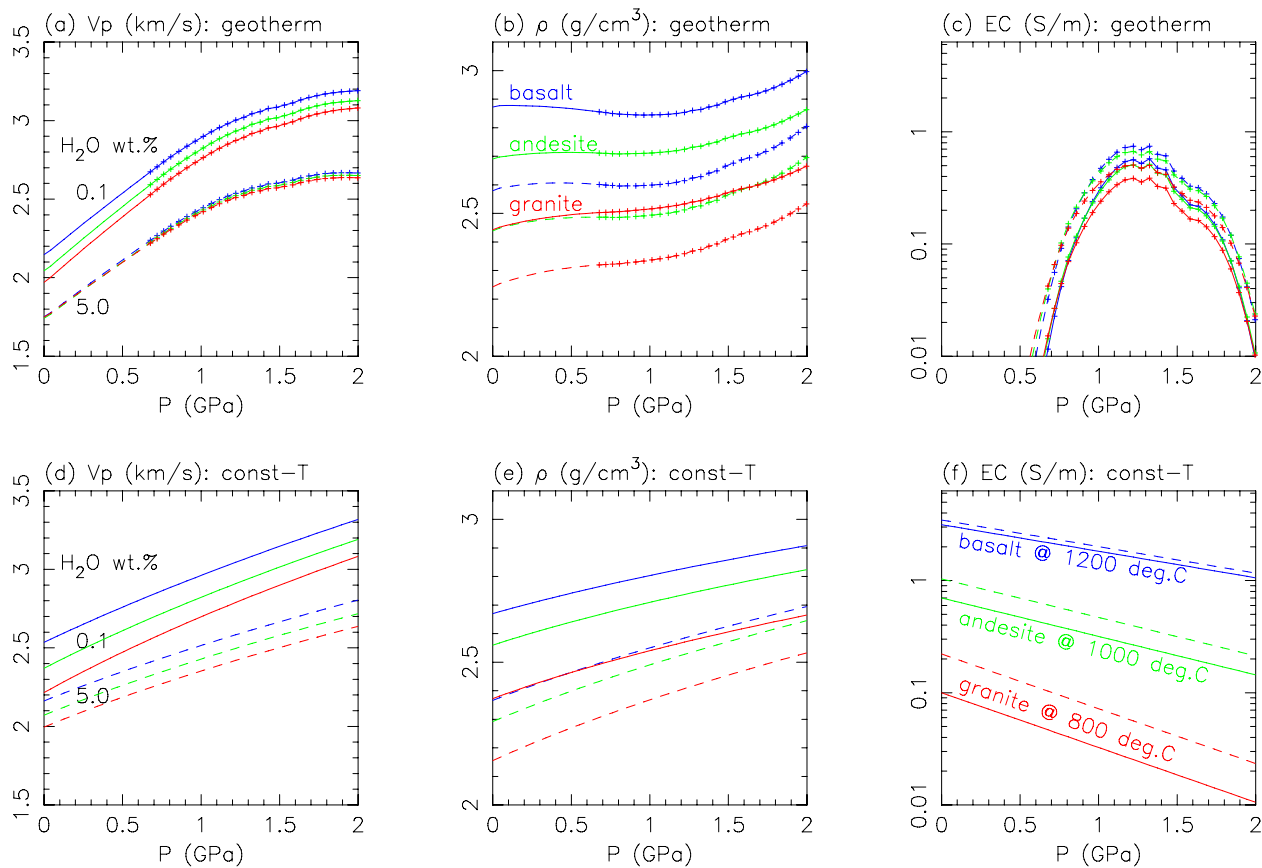


**Figure 7.** Physical properties of silicate melts, based on Ueki and Iwamori (2016) and Pommier and Le-Trong (2011), for basalt (Iwate basalt, IW17,  $\text{SiO}_2 = 51.38 \text{ wt.\%}$ ,  $\text{Na}_2\text{O} = 1.91 \text{ wt.\%}$ , Ueki & Iwamori, 2016), andesite (Hachimantai andesite, HM01,  $\text{SiO}_2 = 60.86 \text{ wt.\%}$ ,  $\text{Na}_2\text{O} = 2.61 \text{ wt.\%}$ , Ueki & Iwamori, 2016), and granite (Oguni fine-grained biotite granite, 03060302,  $\text{SiO}_2 = 72.42 \text{ wt.\%}$ ,  $\text{Na}_2\text{O} = 3.46 \text{ wt.\%}$ , Kamei et al., 2015) melts with  $\text{H}_2\text{O}$  concentrations of 0.1 and 5.0 wt.\%. The upper row (a–c) represents the physical properties along the geotherm shown in Figure 1b, in which the properties above 973 K are represented by the plus symbol. The solid lines represent the cases with 0.1 wt.\%  $\text{H}_2\text{O}$ , and the broken lines represent those with 5.0 wt.\%  $\text{H}_2\text{O}$ . The lower row (d–f) represents those at constant temperatures; 1,473 K (1,200°C, blue line) for basaltic melt, 1,273 K (1,000°C, green line) for andesitic melt, and 1,073 K (800°C, red line) for granitic melt.

$$\frac{\Delta V_s}{V_s^0} = \left[ \Lambda_N - \left( 1 - \frac{\rho_L}{\rho_s} \right) \right] \frac{\phi}{2} \quad (2)$$

where  $V_p^0 = \sqrt{(K_s + 4\mu_s/3)/\rho_s}$ ,  $V_s^0 = \sqrt{\mu_s/\rho_s}$ ,  $\beta = K_s/K_p$ ,  $\gamma = \mu_s/K_s$ ,  $K$  is the bulk modulus,  $\mu$  is the shear modulus,  $\rho$  is the density, and  $\phi$  is the volume fraction of liquid. The subscripts  $s$ ,  $l$ , and  $b$  represent the solid, liquid, and bulk mixture, respectively.  $\Lambda_{K_b}$  and  $\Lambda_N$  represent the slopes of  $\phi - K_b/K_s$  and  $\phi - \mu_b/\mu_s$  relations that involve the effect of pore shapes (represented by the aspect ratio  $\alpha$ ), respectively, as shown in Figure 2 of Takei (2002).

On the basis of the physical properties for the individual solid and liquid phases described in the previous sections,  $V_p$  and  $V_s$  of the mixture were calculated for various lithologies with aqueous fluid or melt at a given  $P$ - $T$ - $\phi$ - $\alpha$ . Figure 8 exhibits an example of a mixture of gabbro and aqueous fluid at  $P = 1.0 \text{ GPa}$  and  $T = 1,000 \text{ K}$ . Both  $V_p$  and  $V_s$  decrease linearly with increasing  $\phi$  (hence a rapid velocity decrease against log-scaled  $\phi$ ). The dependence of  $V_p$ - $\phi$  and  $V_s$ - $\phi$  relations on  $\alpha$  is shown in Figure 9. Here, a mixture of gabbro and basaltic melt at  $P = 1.0 \text{ GPa}$  and  $T = 1,473 \text{ K}$  (red lines in Figure 9), as well as a mixture of the gabbro and an aqueous fluid at  $P = 1.0 \text{ GPa}$  and  $T = 1,000 \text{ K}$  (black lines in Figure 9) are shown. When  $\alpha$  is small (e.g.,  $10^{-5}$  and a small fraction of the liquid phase may develop fully connected cracks),  $V_p$  and  $V_s$  start to decrease at a low  $\phi$  comparable to the  $\alpha$  value. Meanwhile, the decrease in  $V_p$  and  $V_s$  occurs at a relatively

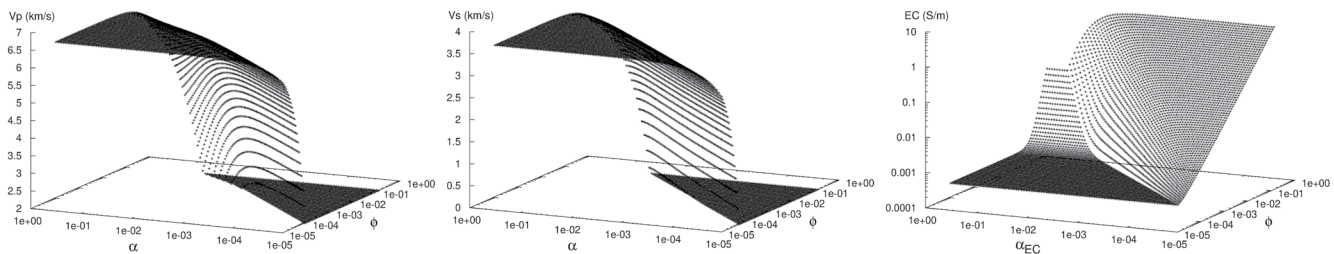


**Figure 8.** Seismic velocities ( $V_p$ , left;  $V_s$ , middle) and electrical conductivity (EC, right) of a mixture of rock (gabbro “12\_gbr” in Table 1) and aqueous fluid at  $P = 1.0$  GPa,  $T = 1,000$  K, for the wide range of  $\phi$ ,  $\alpha$ , and  $\alpha_{EC}$  from  $10^{-5}$  to 1,  $10^{-5}$  to 1, and  $10^{-5}$  to 1, respectively. The density of melt was calculated as in Section 2.3 based on Ueki and Iwamori (2016), whereas the densities of 20 rock suites were approximated as follows: “amp” = 2.9 ( $10^3$  kg/m $^3$ ), “ecl” = 3.4, “gbr” = 3.0, “gns” = 2.8, “grd” = 2.8, “grl” = 2.9, “grn” = 2.7, “hbd” = 2.9, “hrz” = 3.3, “hyu” = 2.9, “kzg” = 2.7, “lhr” = 3.3, “mgm” = 2.7, “mrb” = 2.9, “myl” = 2.7, “pel” = 2.9, “qtz” = 2.7, “sed” = 2.5, “ton” = 2.8, “lim” = 2.7. These density values were used to calculate  $\rho_L/\rho_S$  in Equations 1 and 2, where the uncertainties in  $\rho_L/\rho_S$  and the approximated rock density have negligible effects on the results (Takei, 2002).

large  $\phi$  when  $\alpha$  is large (e.g., 0.1, for connected tubes along the grain boundary as an equilibrium texture). Notably, the solid–melt mixture exhibits appreciably higher  $V_p$  than the solid–aqueous fluid mixture, particularly when  $\phi > \sim 0.01$ , whereas both mixtures exhibit nearly the same  $V_s$ , which reflects the distinct bulk modulus of the melt and aqueous fluid.

The effective electrical conductivity of the mixture also depends strongly on the geometry and connectivity of the liquid phase. Various theoretical and empirical models have been proposed, as shown in Table 1 of Glover et al. (2000), including simple geometrical models (e.g., parallel layers arranged axially or normally to current flow), theoretical upper/lower bounds based on Hashin and Shtrikman (1963), and experiment-based empirical equations (e.g., Archie’s law, Archie, 1942; modified Archie’s law, Glover et al., 2000). Among the simple geometrical models, the effective bulk conductivity ( $\sigma_b$ ) of a parallel model with liquid layers arranged parallel to the current flow is expressed as

$$\sigma_b = f\phi\sigma_l + (1 - \phi)\sigma_s \quad (3)$$

where,  $\sigma_l$  and  $\sigma_s$  are the electrical conductivities of the liquid and solid, respectively, and the factor  $f$  is unity for the parallel model. For other fluid geometries, for instance, a tube or sheet/film network developed along the edge or side of solid grains,  $f$  is 1/3 or 2/3. When  $\sigma_l \gg \sigma_s$ ,  $\sigma_b$  is almost proportional to  $\phi$ , whereas the Archie’s equation includes a power law of  $\phi$ , regarded as representing cementation at low  $\phi$  (Archie, 1942). Archie’s law was originally developed for sedimentary rocks of oil and gas reservoirs, and has been found to be applicable to partial molten rocks (ten Grotenhuis et al., 2005; Watanabe & Kurita, 1993).

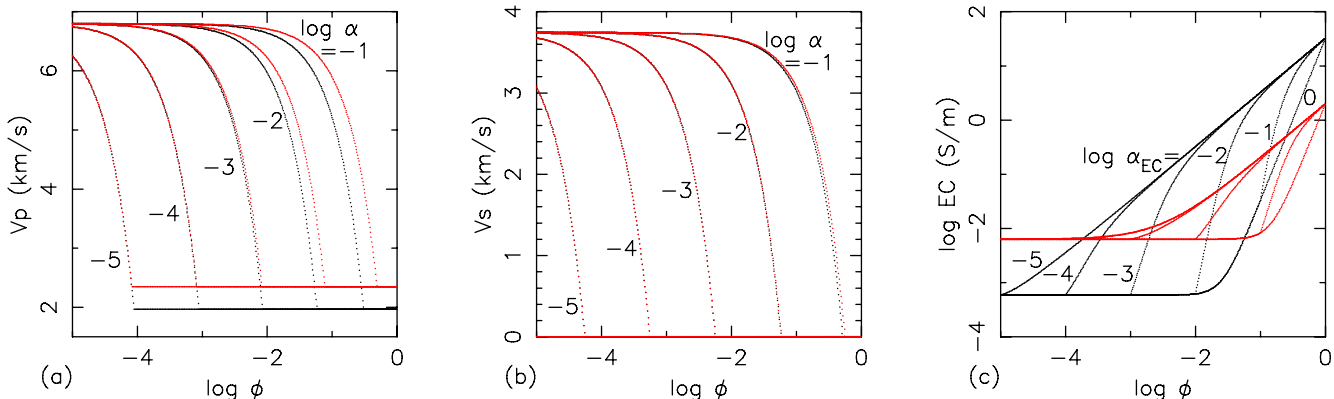


**Figure 9.** Seismic velocities (a)  $V_p$ , (b)  $V_s$ , and (c) electrical conductivity  $\sigma_b$  (EC) of a mixture of rock (gabbro, no. 65 “12\_gbr” in Table 1) and saline aqueous fluid of 5 wt.% NaCl at  $P = 1.0$  GPa,  $T = 1,000$  K (black lines), and a mixture of the same rock and basaltic melt at  $P = 1.0$  GPa,  $T = 1,473$  K (red lines). In panels (a) and (b), the effect of pore shape is represented by the aspect ratio  $\alpha$  (Takei, 2002), e.g.,  $\alpha$  less than  $\sim 10^{-3}$  corresponds to cracks and  $V_p$  and  $V_s$  reduce significantly above  $\phi$  greater than  $\sim 10^{-3}$ .  $\alpha \sim 0.1$ –0.5 corresponds to tube along the grain edges. In panel (c)  $\alpha_{EC}$  represents the critical  $\phi$ , above which  $\sigma_b$  increases largely with a small increase in  $\phi$ . The base curve labeled “0” in this example was calculated based on the modified Archie’s law (Glover et al., 2000) with the exponent  $m = 3$ .

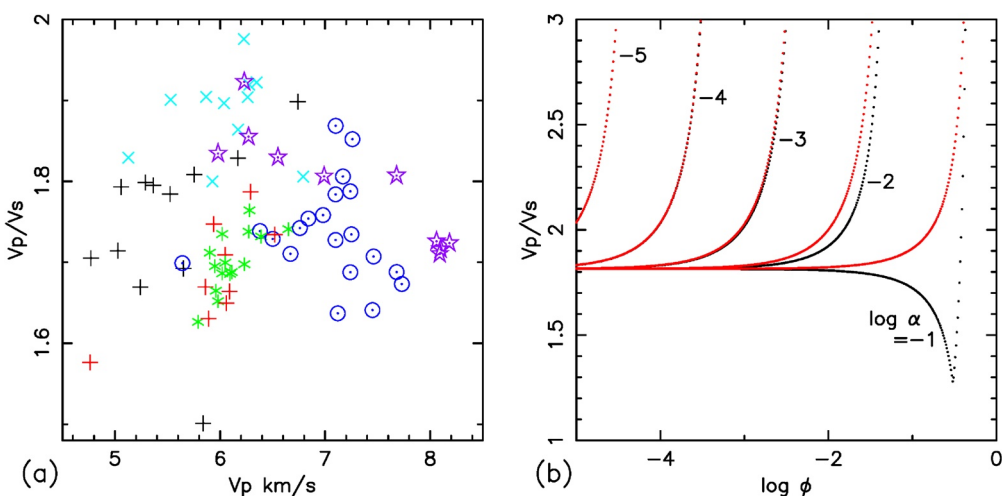


**Figure 10.**  $V_p/V_s$  ratio for (a) the various lithologies (Table 1) at 0.001 GPa and 273 K, where sedimentary rock (black cross), limestone (sky-blue cross), felsic igneous/metamorphic rock (red cross), intermediate rock (green asterisk), mafic rock (blue circle), and ultramafic rock (purple star). (b) The mixture of gabbro and liquid phase with the same condition as in Figure 9 (saline aqueous fluid [black dotted line] and basaltic melt [red dotted line]) with variable liquid fraction  $\phi$  and geometry represented by the pore aspect ratio  $\alpha$ .

The modified Archie's law accounts for the electrical conductivity at low  $\phi$ , which approaches that of the solid. It also accounts for the fluid-dominant regime at relatively high  $\phi$ , which approaches the conventional Archie's law for the same given exponent  $m$  (Glover et al., 2000). The transition from the low-  $\phi$  to high-  $\phi$  regime occurs rather rapidly with an increase in  $\phi$ , particularly when  $m$  is relatively large (e.g., the curve labeled "0" in Figure 9c). Such a rapid transition may occur even at a low- $\phi$  condition if fluid-filled cracks develop to form an interconnected network (e.g., Watanabe et al., 2019), which can be treated as a problem of percolation (Guéguen & Palciauskas, 1994). When the crack density or fluid fraction becomes higher than a critical value (percolation threshold), an interconnected crack network is rapidly formed, resulting in a large  $\sigma_b$  with a small increase in  $\phi$  (Dienes, 1982; Guéguen & Dienes, 1989; Watanabe, 2005). This rapid change around the critical fluid fraction was quantitatively modeled assuming the Bethe lattice for the liquid network (Dienes, 1982; Guéguen & Dienes, 1989) and is approximated by the following equation using the hyperbolic tangent function to converge to Equation 3 for the parallel layer model with  $f = 1$  at  $\phi$  sufficiently higher than the critical liquid fraction represented by the parameter  $\alpha_{EC}$ :

$$\log \sigma_b = \log \sigma_1 + \log(\sigma_1/\sigma_2) \tanh\{\log(\phi/\alpha_{EC})\}^2 \quad (4)$$

where  $\sigma_1$  and  $\sigma_2$  correspond to the electrical conductivity at the critical fraction  $\alpha_{EC}$  and the electrical conductivity according to the parallel model at a given  $\phi$ , respectively.

Figure 9c shows examples of the  $\phi-\sigma_b$  relation for the variable critical value  $\alpha_{EC}$  for a rock-saline aqueous fluid system (at 1 GPa and 1,000 K) and rock-melt system (at 1 GPa and 1,473 K). Both systems exhibit an appreciable increase (maximum  $\sim 3$  orders of magnitude) in  $\sigma_b$  with a small increase in  $\phi$ . Thus, such a behavior needs to be considered when discussing the crustal structure in subduction zones (e.g., Figure 1) where cracks and faults can be densely distributed and associated with high seismicity and crustal deformation. The connectivity of cracks or faults is characterized by  $\alpha_{EC}$ : a fluid network with higher connectivity has a lower  $\alpha_{EC}$ .

### 3. Necessity and Utility of the Combined Forward Model

For interpreting seismic velocity structures, the  $V_p/V_s$  ratio is commonly referred to as a key parameter in the lithology, as well as the presence of fluid phases (e.g., Brantut & David, 2019; Christensen, 1996; Fortin et al., 2007; Le Ravalec & Guéguen, 1996; O'Connell & Budiansky, 1974; Takei, 2002; Watanabe, 1993). The  $V_p/V_s$  ratio of various lithologies at a near-surface condition ranges from approximately 1.5 to 2.0

**Table 3**

Synthetic Data Based on the Seismic and Magnetotelluric Observations Shown in Figure 1

No. in Table 1	Lithology	Liquid	P (GPa)	T (K)	$\log_{10}\phi$ (x100)	$\log_{10}\alpha$ (x100)	$\log_{10}\alpha_{EC}$ (x100)	$\phi$	$\alpha$	$\alpha_{EC}$	$V_p$ (km/s)	$V_s$ (km/s)	$\sigma$ (S/m)
26	30_grn	Aqueous fluid	0.1325	393.349	-176	-92	-186	0.017378	0.120226	0.013804	5.680	3.410	5.82E-04
45	07_grd	Aqueous fluid	0.1988	465.034	-314	-244	-362	0.000724	0.003631	0.00024	6.121	3.488	4.61E-03
48	28_gbr	Aqueous fluid	0.1988	465.034	-226	-172	-262	0.005495	0.019055	0.002399	6.142	3.481	3.10E-03
66	11_amp	Melt	0.5446	824.518	-94	-10	-124	0.114815	0.794328	0.057544	6.541	3.820	2.41E-04
67	13_gbr	Melt	0.6917	968.588	-200	-106	-206	0.01	0.087096	0.00871	6.820	3.910	4.87E-04
75	16_lhr	Melt	1.1626	1,318.93	-214	-142	-228	0.007244	0.038019	0.005248	7.690	4.340	1.58E-03

Note. Different lithologies (30\_grn [no. 26 granite in Table 1], 07grd [no. 45 granodiorite], 28\_gbr [no. 48 gabbro], 11\_amp [no. 66 amphibolite], 13\_gbr [no. 67 gabbro], 16\_lhr [No. 75 lherzolite]) and the two liquid phases (aqueous fluid with 5 wt.% NaCl and basaltic melt of 51 wt.% SiO<sub>2</sub>) were selected to consider conditions ranging from the shallow crust to the uppermost mantle.

(Figure 10a). Figure 10a also displays that an appreciable range in the  $V_p/V_s$  ratio exists even for a relatively restricted lithology (e.g., limestone, felsic/intermediate/mafic igneous rock, ultramafic rock) depending on the precise composition or degree of hydration. In addition, the presence of fluid in the grain boundaries, pores, and cracks strongly modifies the  $V_p/V_s$  ratio in a variable manner (Figure 10b), including the effects of compressibility and pore geometry of the liquid phase (Brantut & David, 2019; Takei, 2002; Watanabe, 1993). Although the  $V_p/V_s$  ratio of the liquid-solid mixture generally increases with increasing liquid fraction  $\phi$ , the  $V_p/V_s$  ratio may decrease with a pore shape close to equilibrium geometry ( $\log \alpha \approx -1$ ) at relatively high liquid fractions ( $\log \phi \approx -2$  to  $-0.5$ ) for the mixture of saline aqueous fluid and gabbro (Figure 10b). On the other hand, the mixture of melt and gabbro does not exhibit such a decrease in  $V_p/V_s$  owing to the less compressible nature of the melt, which is distinct from aqueous fluid. These variations in  $V_p/V_s$  suggest that, to evaluate the lithology and the effects of the liquid phase based on geophysical observations, the seismic velocity alone would not provide sufficient constraints on the crust-uppermost mantle structure. Thus, electrical conductivity also needs to be utilized simultaneously. To investigate whether such an evaluation is quantitatively possible and to exhibit the utility of the forward model combining seismic velocity and conductivity, the present study sets several synthetic data, based on the seismic and MT observations shown in Figure 1, including different lithologies and liquid phases (Table 3).

### 3.1. Misfit Distribution Over the Parameter Space

To examine the relationship between the observable variables (i.e., seismic velocities and electrical conductivity) and the model parameters (i.e., lithology, liquid phase [aqueous fluid or melt], and liquid fraction with geometrical parameters), we define the misfit function  $r$  as follows:

$$r = \left[ (V_{P\_calc} - V_{P\_true})/\Delta V_P \right]^2 + \left[ (V_{S\_calc} - V_{S\_true})/\Delta V_S \right]^2 + \left[ \log_{10}(\sigma_{calc}/\sigma_{true})/\Delta\sigma \right]^2 \quad (5)$$

where  $\Delta V_P$ ,  $\Delta V_S$ , and  $\Delta\sigma$  represent the standard deviations of the observational uncertainties as weight factors for the least squares residual, and  $\Delta V_P = 0.03 V_{P\_true}$ ,  $\Delta V_S = 0.03 V_{S\_true}$ , and  $\Delta\sigma = 0.5$ , respectively (Ogawa et al., 2014; Okada et al., 2014). We then mapped the misfit  $r$  from the exact solution over the discretized parameter space. Figure 11 shows such a map in the parameter space of  $\phi$ - $\alpha$ - $\alpha_{EC}$  for granodiorite with saline aqueous fluid (no. 45 “07\_grd” in Table 3). The distribution of  $r$  on the  $\alpha$ - $\alpha_{EC}$ ,  $\phi$ - $\alpha_{EC}$ , and  $\phi$ - $\alpha$  planes (Figures 11a–11c) shows complex surfaces with a deep hole that corresponds to the global minimum in the parameter space (Figure 11d). The deep holes of misfit minimum are not strongly elongated along a specific direction, indicating that the sensitivity to search for the minimum is relatively high and uniform with respect to the liquid parameters.

In Figure 11d, some positive correlations among  $\phi$ ,  $\alpha$ , and  $\alpha_{EC}$  are observed for the low-misfit zones (e.g.,  $r < 0.01$ ). In addition, a combination of higher  $\phi$ - $\alpha$ - $\alpha_{EC}$  and a combination of lower  $\phi$ - $\alpha$ - $\alpha_{EC}$  may fit the synthetic true solution with a similarly low  $r$ . As shown in Figure 9, the effects of a higher  $\phi$  with fixed values

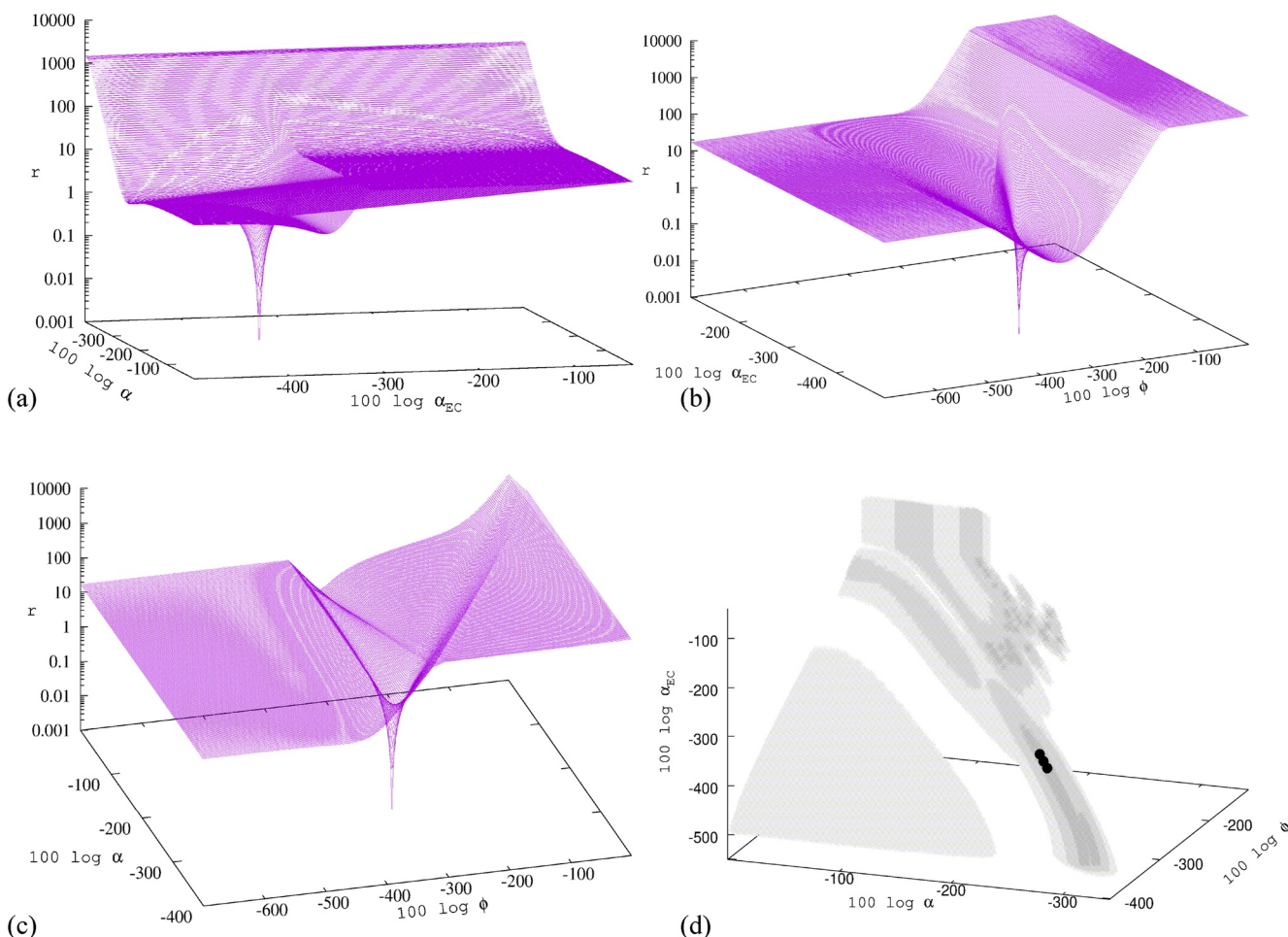


**Figure 11.** Distribution of misfit  $r$  around the synthetic true solution for 07\_grd (no. 45 granodiorite in Table 3) in the parameter space of  $\phi$ - $\alpha$ - $\alpha_{EC}$ . The misfit was defined in the main text and was calculated over the parameter space discretized with a sufficiently fine grid (node interval of 0.01 for  $\log_{10}\phi$ ,  $\log_{10}\alpha$ , and  $\log_{10}\alpha_{EC}$ ) to resolve the global minimum. The three diagrams of the upper left (a), upper right (b), and lower left (c) show the distribution of  $r$  on the  $\alpha$ - $\alpha_{EC}$ ,  $\phi$ - $\alpha_{EC}$ , and  $\phi$ - $\alpha$  planes, respectively, in which the plot range of  $z$ -axis ( $r$ ) below 0.001 is cut off for clarity. Distribution of  $r$  in the  $\phi$ - $\alpha$ - $\alpha_{EC}$  volume (lower right diagram [d]) are color coded into four volumes that correspond to  $r < 0.3$  (the palest gray),  $r < 0.1$ ,  $r < 0.01$ , and  $r < 0.0004$  (black), respectively.

of  $\alpha$  and  $\alpha_{EC}$  on the seismic velocity and electrical conductivity (i.e., decrease in  $V_p$  and  $V_s$ , and increase in  $\sigma$  due to the presence of the liquid phase) may be reproduced by a lower  $\phi$  together with a lower  $\alpha$  and  $\alpha_{EC}$ , which effectively enhance the liquid effects. This accounts for the positive correlation between  $\phi$ ,  $\alpha$ , and  $\alpha_{EC}$  in Figure 11d. It should be noted that, despite the correlation, the global minimum is found in Figure 11d.

All the lithologies in Table 1 and the liquid phases were examined to calculate the misfit (i.e., 78 lithologies including “07\_grd” that corresponds to the synthetic true solution, combined with either aqueous fluid or melt). Similar structures can be found for other lithologies and liquid phases, and the combination of lithology-liquid phase- $\phi$ - $\alpha$ - $\alpha_{EC}$  to minimize  $r$  can be found by calculating the misfit over the parameter space; the synthetic sets of lithology-liquid phase- $\phi$ - $\alpha$ - $\alpha_{EC}$  in Table 3 were recovered based on the set of  $P$ ,  $T$ ,  $V_p$ ,  $V_s$ , and  $\sigma$  (Table 3) by the grid search method (i.e., discretizing the parameter space with a multidimensional grid, including the arbitrary choice of lithology and liquid phase, and calculating  $r$  at each grid-node to find the minimum). This can also be explored by other methods such as Markov Chain Monte Carlo (MCMC) methods, provided that an appropriate Likelihood function is defined with the prior information.

In this numerical experiment, the number of unknown parameters is five for lithology-liquid phase- $\phi$ - $\alpha$ - $\alpha_{EC}$ , and the unknowns are constrained by the five parameters consisting of a given set of  $P$ ,  $T$ ,  $V_p$ ,  $V_s$ , and  $\sigma$ .

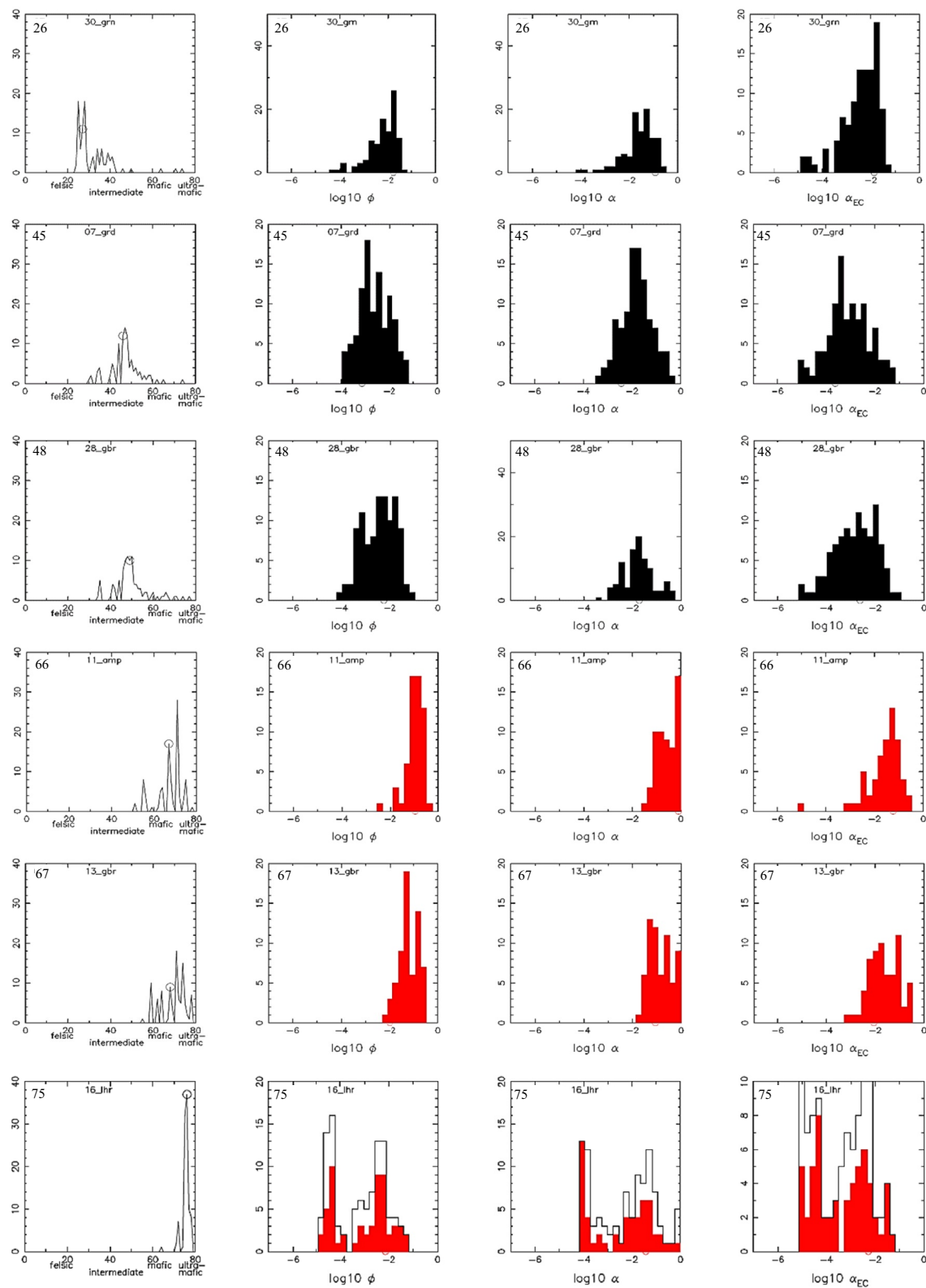


**Figure 12.**

The chemical composition of liquid phase is assumed, i.e., aqueous fluid with 5 wt.% NaCl or a basaltic melt of 51 wt.% SiO<sub>2</sub>, with which the system in this experiment is completely described with a unique solution.

### 3.2. Inversion Test of Perturbed Velocity-Conductivity Data by Grid Search

To examine how the minimization for finding the solution is affected by the observational uncertainties, we perturbed the individual synthetic data (Table 3) using Gaussian noise with standard deviations of  $\Delta V_p = 0.03 V_{p\_true}$ ,  $\Delta V_s = 0.03 V_{s\_true}$ , and  $\Delta \sigma = 0.5$ , which correspond to the observational uncertainties in the seismic and MT tomography (Ogawa et al., 2014; Okada et al., 2014). We produced 100 sets of perturbed  $V_p$ ,  $V_s$ , and  $\sigma$ , and then used them to search for 100 new solutions of lithology-liquid phase- $\phi$ - $\alpha$ - $\alpha_{EC}$  by minimizing the misfit. Figure 12 shows the frequency distributions of the solutions. For example, the first row corresponds to the solutions for the perturbed data of granite “30\_grn” (no. 26) under the upper crustal condition (Table 3), and the left column displays the lithology solutions obtained from felsic (left hand side) to mafic (right-hand side). The aqueous fluid phase, rather than the melt phase, was found to minimize the misfit in all these “30\_grn” solutions, which are distributed around the synthetic true solution with some scatter toward more mafic lithologies. Accordingly, the  $\phi$ - $\alpha$ - $\alpha_{EC}$  of the aqueous fluid phase also exhibits variability and scatter around the synthetic true solution (top row, Figure 12). Similar variability is found for the noise-perturbed data of intermediate and mafic lithologies (no. 45 “07\_grd” and no. 48 “28\_gbr”) with aqueous fluid phase under the middle crustal condition; the 100 solutions exhibit the lithological variation from intermediate to mafic and a standard deviation of approximately an order of magnitude in  $\phi$ - $\alpha$ - $\alpha_{EC}$  (second and third rows of Figure 12).

The remaining three examples in Figure 12 (lower three rows) involve a mixture of melt and mafic/ultramafic lithologies at relatively elevated pressures and temperatures that correspond to the lower crustal and uppermost mantle conditions. The results for the mixture of amphibolite and 11% basaltic melt (no. 66 “11\_amp” in Table 3) are distributed around the synthetic true solution within a relatively narrow range in  $\phi$ - $\alpha$ - $\alpha_{EC}$ , although the lithologies are distributed from intermediate to ultramafic. When  $\phi$  is small, the velocities mostly determine the lithology (e.g., no. 45 “07\_grd” in Figure 12), and if  $\phi$  increases (e.g., no. 66 “11\_amp”), the lithology estimates tend to scatter while the liquid parameters tend to be constrained better.

For the gabbro-melt mixture (no. 67 “13\_gbr”), the lithologies corresponding to the perturbed data are distributed from intermediate to ultramafic, and the  $\phi$  distribution is skewed toward higher  $\phi$  partly due to the lithological variability. However, the results for peridotite (no. 75 “16\_lhr”) exhibit limited ultramafic lithologies around the synthetic true solution of lherzolite but, at the same time, relatively wide ranges in  $\phi$ - $\alpha$ - $\alpha_{EC}$ . Of the 100 noise-perturbed cases for “16\_lhr,” the melt phase was identified as the optimal liquid phase in 56 cases, whereas the aqueous fluid phase was identified in the remaining 44 cases. This indicates that the optimal liquid phase and the related parameters are significantly affected by the noise, resulting in relatively wide ranges in  $\phi$ - $\alpha$ - $\alpha_{EC}$ .

The examples shown in Figure 12 suggest that information concerning the “true” solution can be extracted from the observable data with uncertainties that are broadly reflected in the variability in the optimized solutions. For instance, the 3%-perturbed  $V_p$  of dry granodiorite under the mid-crustal condition (no. 45 “07\_grd” in Table 3) is  $6.25 \pm 0.19$  km/s and is compared with the  $V_p$  of the dry intermediate to mafic lithologies (Table 1). This broadly corresponds to the lithological variability found in Figure 12. Such behaviors suggest that stochastic approaches would be straightforward and effective for evaluating geological constituents (i.e., to quantify the probability concerning the lithology, liquid phase, and their proportions) of the crust and the uppermost mantle based on the seismic velocities and electrical conductivity. In the future work, we will discuss such methods based on Bayesian statistics.

In the examples shown in Figures 11 and 12, the five parameters of lithology-liquid phase- $\phi$ - $\alpha$ - $\alpha_{EC}$  have been constrained from the three observable variables with pressure and temperature. In addition to these

**Figure 12.** Best fit solutions in terms of lithology (left column) and parameters of liquid phase ( $\phi$ ,  $\alpha$ ,  $\alpha_{EC}$ ) from the second left column to right, for aqueous fluid (black) or melt (red) for the synthetic data that were normally perturbed by 3% for  $V_{p\_true}$  and  $V_{s\_true}$ , and 0.5 for  $\log_{10}\sigma_{true}$ . The synthetic true solutions are shown by a full circle for lithology (left column) or by small half circles along the horizontal axis for  $\phi$ ,  $\alpha$ , and  $\alpha_{EC}$ . One hundred sets of perturbed ( $V_p$ ,  $V_s$ ,  $\sigma$ ) were examined to find the best fit solutions. The frequency diagrams for  $\phi$ ,  $\alpha$ ,  $\alpha_{EC}$  of the bottom row include the aqueous fluid solutions (black lines) in addition to the melt solutions (red filled bars).

five parameters, more unknown parameters exist in the form of pressure, temperature, and chemical composition of the liquid phase. Although it is possible to explore such a problem, a realistic approach would be to increase the independent constraints on the parameters as prior information. In Figures 11 and 12, the pressure and temperature were estimated based on the numerical simulation of the subduction zone (Figure 1). In addition, the petrological and geochemical observations for the deep-seated brine and erupted magma were used to constrain the compositions of the aqueous fluid and melt, as described.

Various attempts to increase the constraints for investigating the crust-upper mantle structure and distribution of geofluids have been incorporated so far: for example, imaging the deep structure beneath a mid-ocean ridge based on seismic/electromagnetic observations and the anisotropic structure (The MELT Seismic Team, 1998), and comparisons among the geological cross-section, depth-migrated reflection profile, seismic wave, and resistivity tomography of the North American continental lithosphere (Hammer et al., 2011). Nakajima et al. (2005) combined the seismic velocities and attenuation to quantify the liquid fraction in the mantle wedge beneath the northeast Japan arc, assuming that the liquid phase is a melt. The impact of liquid-filled pores and cracks on anisotropy and dispersion of elastic properties of rocks has been demonstrated experimentally and theoretically (e.g., Adelinet et al., 2011; X.-Q. Wang et al., 2012). Within this context, the model presented in this study contributes to such imaging by quantifying the lithology and liquid phase parameters. This model can be tested and calibrated with industrial data in which physical well-logging/deep drilling and precise physical properties for specific lithologies are available (e.g., Carcione et al., 2007; Elbra et al., 2011). This can also be applied to the deeper crust-upper mantle, incorporating anisotropy, attenuation, and density-gravity into the model.

#### 4. Summary

We present a forward model to quantify the  $V_p$ ,  $V_s$ , and  $\sigma$  of the solid-liquid mixtures based on previously published experimental and theoretical studies on the seismic velocity and electrical conductivity of solid rocks and liquid phases (aqueous fluid and melt). For a given set of pressure, temperature, lithology, liquid phase, liquid fraction, and the geometrical parameters related to the aspect ratio and connectivity of the liquid phase,  $V_p$ ,  $V_s$ , and  $\sigma$  were calculated corresponding to the lithologies and conditions appropriate for the crust and the uppermost mantle. That is, a total of 78 felsic to ultramafic lithologies, aqueous fluid with ~0–10 wt.% NaCl, mafic to felsic melt, and their mixture properties were modeled to calculate  $V_p$ ,  $V_s$  and  $\sigma$  over the pressure range from 0 to 2 GPa and the temperature range from 273 to ~1,600 K. This forward model may be used to inversely estimate the lithology, liquid phase, liquid fraction, and the geometrical parameters of the liquid phase, based on the observed  $V_p$ ,  $V_s$ , and  $\sigma$ , by minimizing the misfit between the calculated  $V_p$ - $V_s$ - $\sigma$  and observed  $V_p$ - $V_s$ - $\sigma$ . Analyses of the misfit distribution over the parameter space and the noise-perturbed data suggest that the forward model would be useful for solving such inversion problems with prior information on the geothermal structure and composition of the liquid phase.

#### Data Availability Statement

For the data policy, all of the data are available through Hughes and Cross (1951), Miller and Stewart (1990), Kern and Tubia (1993), Kern and Schenk (1988), Kern et al. (1999, 2002), Matsukage et al. (2005), Punturo et al. (2005), D. Wang et al. (2005), Kono et al. (2006), Nishimoto et al. (2008), Mirwald (1979), Fuji-ta et al. (2004, 2007, 2011), D. Wang et al. (2008), Reynard et al. (2011), Ogawa et al. (2014), Okada et al. (2014), Kamei et al. (2015), and Ueki and Iwamori (2016).

#### References

- Adelinet, M., Fortin, J., & Guégan, Y. (2011). Dispersion of elastic moduli in a porous-cracked rock: Theoretical predictions for squirt-flow. *Tectonophysics*, 503, 173–181. <https://doi.org/10.1016/j.tecto.2010.10.012>
- Archie, G. E. (1942). The electrical resistivity log as an aid in determining some reservoir characteristics. *Transactions of the American Institute of Mining, Metallurgical and Petroleum Engineers*, 146, 54–62. <https://doi.org/10.2118/942054-G>
- Bannard, J. E. (1975). Effect of density on the electrical conductance of aqueous sodium chloride solutions. *Journal of Applied Electrochemistry*, 5(1), 43–53. <https://doi.org/10.1007/bf00625958>

- Birch, F. (1947). Finite elastic strain of cubic crystals. *Physical Reviews*, 71, 809–824. <https://doi.org/10.1103/PhysRev.71.809>
- Brantut, N., & David, E. C. (2019). Influence of fluids on  $V_p/V_s$  ratio: Increase or decrease? *Geophysical Journal International*, 216, 2037–2043. <https://doi.org/10.1093/gji/ggy518>
- Brenan, J. M., Shaw, H. F., Ryerson, F. J., & Phinney, D. L. (1995). Mineral-aqueous fluid partitioning of trace elements at 900°C and 2.0 GPa: Constraints on the trace element chemistry of mantle and deep crustal fluids. *Geochimica et Cosmochimica Acta*, 59, 3331–3350. [https://doi.org/10.1016/0016-7037\(95\)00215-1](https://doi.org/10.1016/0016-7037(95)00215-1)
- Carcione, J. M., Ursin, B., & Nordskag, J. I. (2007). Cross-property relations between electrical conductivity and the seismic velocity of rocks. *Geophysics*, 72, 193–204. <https://doi.org/10.1190/1.2762224>
- Christensen, N. I. (1996). Poisson's ratio and crustal seismology. *Journal of Geophysical Research*, 101(B2), 3139–3156. <https://doi.org/10.1029/95jb03446>
- Christensen, N. I., & Fountain, D. M. (1975). Constitution of the lower continental crust based on experimental studies of seismic velocities in granulite. *Geological Society of America Bulletin*, 86, 227–236. [https://doi.org/10.1130/0016-7606\(1975\)86<227:cotlcc>2.0.co;2](https://doi.org/10.1130/0016-7606(1975)86<227:cotlcc>2.0.co;2)
- Dai, L., Hu, H., Li, H., Wu, L., Hui, K., Jiang, J., & Sun, W. (2016). Influence of temperature, pressure, and oxygen fugacity on the electrical conductivity of dry eclogite, and geophysical implications. *Geochemistry, Geophysics, Geosystems*, 17, 2394–2407. <https://doi.org/10.1002/2016GC006282>
- Dai, L., Sun, W., Li, H., Hu, H., Wu, L., & Jiang, J. (2018). Effect of chemical composition on the electrical conductivity of gneiss at high temperatures and pressures. *Solid Earth*, 9, 233–245. <https://doi.org/10.5194/se-9-233-2018>
- Dienes, J. K. (1982). Permeability, percolation and statistical crack mechanics. In R. E. Goodman & F. E. Heuze (Eds.), *Issues in rock mechanics* (pp. 86–94) American Institute of Mining, Metallurgical and Petroleum Engineering.
- Driesner, T. (2007). The system  $H_2O$ -NaCl. Part II: Correlations for molar volume, enthalpy, and isobaric heat capacity from 0 to 1000°C, 1 to 5000 bar, and 0 to 1  $X_{NaCl}$ . *Geochimica et Cosmochimica Acta*, 71(20), 4902–4919. <https://doi.org/10.1016/j.gca.2007.05.026>
- Eberhart-Phillips, D., Stanley, W. D., Rodriguez, B. D., & Lutter, W. J. (1995). Surface seismic and electrical methods to detect fluids related to faulting. *Journal of Geophysical Research*, 100, 12919–12936. <https://doi.org/10.1029/94jb03256>
- Elbra, T., Karlqvist, R., Lassila, I., Häggström, E., & Pesonen, L. J. (2011). Laboratory measurements of the seismic velocities and other petrophysical properties of the Outokumpu deep drill core samples, eastern Finland. *Geophysical Journal International*, 184, 405–415. <https://doi.org/10.1111/j.1365-246x.2010.04845.x>
- Fortin, J., Guéguen, Y., & Schubnel, A. (2007). Effects of pore collapse and grain crushing on ultrasonic velocities and  $V_p/V_s$ . *Journal of Geophysical Research*, 112, B08207. <https://doi.org/10.1029/2005JB004005>
- Fuji-ta, K., Katsura, T., Ichiki, M., Matsuzaki, T., & Kobayashi, T. (2011). Variations in electrical conductivity of rocks above metamorphic conditions. *Tectonophysics*, 504(1), 116–121. <https://doi.org/10.1016/j.tecto.2011.03.008>
- Fuji-ta, K., Katsura, T., Matsuzaki, T., Ichiki, M., & Kobayashi, T. (2007). Electrical conductivity measurement of gneiss under mid-to-lower crustal  $P-T$  conditions. *Tectonophysics*, 434(1), 93–101. <https://doi.org/10.1016/j.tecto.2007.02.004>
- Fuji-ta, K., Katsura, T., & Tainoshio, Y. (2004). Electrical conductivity measurement of granulite under mid-to-lower crustal pressure-temperature conditions. *Geophysical Journal International*, 157(1), 79–86. <https://doi.org/10.1111/j.1365-246X.2004.02165.x>
- Ghiorso, M. S., Hirschmann, M. M., Reiners, P. W., & Kress, V. C., III (2002). The pMELTS: A revision of MELTS for improved calculation of phase relations and major element partitioning related to partial melting of the mantle to 3 GPa. *Geochemistry, Geophysics, Geosystems*, 3(5), 1030. <https://doi.org/10.1029/2001GC002170.1029/2001gc000217>
- Glover, P. W. J., Hole, M. J., & Pous, J. (2000). A modified Archie's law for two conducting phases. *Earth and Planetary Science Letters*, 180(3–4), 369–383. [https://doi.org/10.1016/s0012-821x\(00\)0168-0](https://doi.org/10.1016/s0012-821x(00)0168-0)
- Guéguen, Y., & Dienes, J. (1989). Transport properties of rocks from statistics and percolation. *Mathematical Geology*, 21, 1–13. <https://doi.org/10.1007/bf00897237>
- Guéguen, Y., & Palciauskas, V. (1994). *Introduction to the physics of rocks*. Princeton University Press.
- Hammer, P. T. C., Clowes, R. M., Cook, F. A., Vasudevan, K., & van der Velden, A. J. (2011). The big picture: A lithospheric cross section of the North American continent. *Geological Society of America Today*, 21, 4–10. <https://doi.org/10.1130/gsatg95a.1>
- Hasegawa, A., Yoshida, K., Asano, Y., Okada, T., Iinuma, T., & Ito, Y. (2012). Change in stress field after the 2011 great Tohoku-Oki earthquake. *Journal of Geophysical Research*, 355–356, 231–243. <https://doi.org/10.1016/j.epsl.2012.08.042>
- Hashin, Z., & Shtrikman, S. (1963). A variational approach to the theory of the elastic behaviour of multiphase materials. *Journal of the Mechanics and Physics of Solids*, 11, 127–140. [https://doi.org/10.1016/0022-5096\(63\)90060-7](https://doi.org/10.1016/0022-5096(63)90060-7)
- Horiuchi, S., & Iwamori, H. (2016). A consistent model for fluid distribution, viscosity distribution, and flow-thermal structure in subduction zone. *Journal of Geophysical Research: Solid Earth*, 121, 3238–3260. <https://doi.org/10.1002/2015JB012384>
- Hughes, D. S., & Cross, J. H. (1951). Elastic wave velocities in rocks at high pressures and temperatures. *Geophysics*, 16, 577–593. <https://doi.org/10.1190/1.1437706>
- Ichiki, M., Ogawa, Y., Kaida, T., Koyama, T., Uyeshima, M., Demachi, T., et al. (2015). Electrical image of subduction zone beneath north-eastern Japan. *Journal of Geophysical Research: Solid Earth*, 120, 7937–7965. <https://doi.org/10.1002/2015JB012028>
- Ionov, D. A. (2010). Petrology of mantle wedge lithosphere: New data on supra-subduction zone peridotite xenoliths from the Andesitic Avacha Volcano, Kamchatka. *Journal of Petrology*, 51(1–2), 327–361. <https://doi.org/10.1093/petrology/egp090>
- Ishimaru, S., & Arai, S. (2008). Arsenide in a metasomatized peridotite xenolith as a constraint on arsenic behavior in the mantle wedge. *American Mineralogist*, 93(7), 1061–1065. <https://doi.org/10.2138/am.2008.2746>
- Iwamori, H. (1998). Transportation of  $H_2O$  and melting in subduction zones. *Earth and Planetary Science Letters*, 160, 65–80. [https://doi.org/10.1016/s0012-821x\(98\)00080-6](https://doi.org/10.1016/s0012-821x(98)00080-6)
- Iwamori, H. (2007). Transportation of  $H_2O$  beneath the Japan arcs and its implications for global water circulation. *Chemical Geology*, 239, 182–198. <https://doi.org/10.1016/j.chemgeo.2006.08.011>
- Iwamori, H., & Nakamura, H. (2015). Isotopic heterogeneity of oceanic, arc and continental basalts and its implications for mantle dynamics. *Gondwana Research*, 27, 1131–1152. <https://doi.org/10.1016/j.gr.2014.09.003>
- Kachanov, M., Tsukrov, I., & Shafiro, B. (1994). Effective moduli of solids with cavities of various shapes. *Applied Mechanics Reviews*, 47, 151–174. <https://doi.org/10.1115/1.3122810>
- Kamei, A., Naito, K., Takamura, S., Kagashima, S., Okuzawa, K., Seki, Y., & Watanabe, Y. (2015). Garnet two-mica granite rich in high field strength elements, Kanamaru-Oguni area on the Niigata-Yamagata border, Japan arc. *Japanese Magazine of Mineralogical and Petrological Sciences*, 44, 131–154. <https://doi.org/10.2465/gkk.131211>
- Kawakatsu, H., Kumar, P., Takei, Y., Shinohara, M., Kanazawa, T., Araki, E., & Suyehiro, K. (2009). Seismic evidence for sharp lithosphere-asthenosphere boundaries of oceanic plates. *Science*, 324, 499–502. <https://doi.org/10.1126/science.1169499>

- Kawakatsu, H., & Watada, S. (2007). Seismic evidence for deep-water transportation in the mantle. *Science*, 316, 1468–1471. <https://doi.org/10.1126/science.1140855>
- Kawamoto, T., Yoshikawa, M., Kumagai, Y., Mirabueno, M. H. T., Okuno, M., & Kobayashi, T. (2013). Mantle wedge infiltrated with saline fluids from dehydration and decarbonation of subducting slab. *Proceedings of the National Academy of Sciences USA*, 110, 9663–9668. <https://doi.org/10.1073/pnas.1302040110>
- Keppler, H. (1996). Constraints from partitioning experiments on the composition of subduction-zone fluids. *Nature*, 380, 237–240. <https://doi.org/10.1038/380237a0>
- Kern, H. (1982). P- and S-wave velocities in crustal and mantle rocks under simultaneous action of high confining pressure and high temperature and the effect of the rock microstructure. In W. Schreyer (Ed.), *High-pressure research in geoscience* (pp. 15–45). Schweizerbart.
- Kern, H., Gao, S., Jin, Z., Popp, T., & Jin, S. (1999). Petrophysical studies on rocks from the Dabie ultrahigh-pressure (UHP) metamorphic belt, Central China: Implications for the composition and delamination of the lower crust. *Tectonophysics*, 301, 191–215. [https://doi.org/10.1016/s0040-1951\(98\)00268-6](https://doi.org/10.1016/s0040-1951(98)00268-6)
- Kern, H., Jin, Z., Gao, S., Popp, T., & Xu, Z. (2002). Physical properties of ultrahigh-pressure metamorphic rocks from the Sulu terrain, eastern central China: Implications for the seismic structure at the Donghai (CCSD) drilling site. *Tectonophysics*, 354, 315–330. [https://doi.org/10.1016/s0040-1951\(02\)00339-6](https://doi.org/10.1016/s0040-1951(02)00339-6)
- Kern, H., Popp, T., Gorbatsevich, F., Zharikov, A., Lobanov, K. V., & Smirnov, Y. P. (2001). Pressure and temperature dependence of  $V_p$  and  $V_s$  in rocks from the superdeep well and from surface analogues at Kola and the nature of velocity anisotropy. *Tectonophysics*, 338, 113–134. [https://doi.org/10.1016/s0040-1951\(01\)00128-7](https://doi.org/10.1016/s0040-1951(01)00128-7)
- Kern, H., & Schenk, V. (1988). A model of velocity structure beneath Calabria, southern Italy, based on laboratory data. *Earth and Planetary Science Letters*, 87, 325–337. [https://doi.org/10.1016/0012-821x\(88\)90020-9](https://doi.org/10.1016/0012-821x(88)90020-9)
- Kern, H., & Tubia, J. M. (1993). Pressure and temperature dependence of P- and S-wave velocities, seismic anisotropy and density of sheared rocks from the Sierra Alpujata massif (Ronda peridotites, Southern Spain). *Earth and Planetary Science Letters*, 119, 191–205. [https://doi.org/10.1016/0012-821x\(93\)90016-3](https://doi.org/10.1016/0012-821x(93)90016-3)
- Kern, H., Walther, C., Flüh, E. R., & Marker, M. (1993). Seismic properties of rocks exposed in the POLAR profile region constraints on the interpretation of the refraction data. *Precambrian Research*, 64, 169–187. [https://doi.org/10.1016/0301-9268\(93\)90074-c](https://doi.org/10.1016/0301-9268(93)90074-c)
- Kessel, R., Schmidt, M. W., Ulmer, P., & Pettke, T. (2005). Trace element signature of subduction-zone fluids, melts and supercritical liquids at 120–180 km depth. *Nature*, 437, 724–727. <https://doi.org/10.1038/nature03971>
- Kita, S., Okada, T., Nakajima, J., Matsuzawa, T., & Hasegawa, A. (2006). Existence of a seismic belt in the upper plane of the double seismic zone extending in the along-arc direction at depths of 70–100 km beneath NE Japan. *Geophysical Research Letter*, 33, L24310. <https://doi.org/10.1029/2006GL028239>
- Kobayashi, T., Obata, M., & Yoshimura, Y. (2005). Diatexitite and metatexitite from the Higo metamorphic rocks, west-central Kyushu, Japan. *Journal of Mineralogical and Petrological Sciences*, 100, 1–25. <https://doi.org/10.2465/jmps.100.1>
- Kono, Y., Ishikawa, M., & Arima, M. (2006). Laboratory measurements of P- and S-wave velocities in polycrystalline plagioclase and gabbro-norite up to 700°C and 1 GPa: Implications for the low velocity anomaly in the lower crust. *Geophysical Research Letter*, 33, L15314. <https://doi.org/10.1029/2006GL026526>
- Kuritani, T., Yoshida, T., Kimura, J. I., Hirahara, Y., & Takahashi, T. (2014). Water content of primitive low-K tholeiitic basalt magma from Iwate Volcano, NE Japan arc: Implications for differentiation mechanism of frontal-arc basalt magmas. *Mineralogy and Petrology*, 108, 1–11. <https://doi.org/10.1007/s00710-013-0278-2>
- Kusuda, C., Iwamori, H., Nakamura, H., Kazahaya, K., & Morikawa, N. (2014). Arima hot spring waters as a deep-seated. *Earth, Planets and Space*, 66, 119. <https://doi.org/10.1186/1880-5981-66-119>
- Lange, R. A., & Carmichael, I. S. E. (1987). Densities of  $\text{Na}_2\text{O}\text{-K}_2\text{O}\text{-CaO}\text{-MgO}\text{-FeO}\text{-Fe}_2\text{O}_3\text{-Al}_2\text{O}_3\text{-TiO}_2\text{-SiO}_2$  liquids: New measurements and derived partial molar properties. *Geochimica et Cosmochimica Acta*, 51, 2931–2946. [https://doi.org/10.1016/0016-7037\(87\)90368-1](https://doi.org/10.1016/0016-7037(87)90368-1)
- Lange, R. L., & Carmichael, I. S. E. (1990). Thermodynamic properties of silicate liquids with emphasis on density, thermal expansion and compressibility. *Reviews in Mineralogy and Geochemistry*, 24, 25–64. <https://doi.org/10.1515/9781501508769-006>
- Le Ravalec, M., & Guégan, Y. (1996). High- and low-frequency elastic moduli for a saturated porous/cracked rock–Differential self-consistent and poroelastic theories. *Geophysics*, 61, 1080–1094. <https://doi.org/10.1190/1.1444029>
- Long, M. D., Levander, A., & Shearer, P. M. (2014). An introduction to the special issue of Earth and Planetary Science Letters on USArray science. *Earth and Planetary Science Letters*, 402, 1–5. <https://doi.org/10.1016/j.epsl.2014.06.016>
- Matsukage, K., Nishihara, Y., & Karato, S. (2005). Seismological signature of chemical differentiation of Earth's upper mantle. *Journal of Geophysical Research*, 110, B12305. <https://doi.org/10.1029/2004JB003504>
- Mavko, G. (1980). Velocity and attenuation in partially molten rocks. *Journal of Geophysical Research*, 80, 5173–5189. <https://doi.org/10.1029/jb085ib10p05173>
- Miller, S. L. M., & Stewart, R. R. (1990). Effects of lithology, porosity and shaliness on P- and S-wave velocities from sonic logs. *Canadian Journal of Exploration Geophysics*, 26, 94–103.
- Mirwald, P. W. (1979). The electrical conductivity of calcite between 300 and 1200°C at a  $\text{CO}_2$  pressure of 40 bar. *Physics and Chemistry of Minerals*, 4, 291–297. <https://doi.org/10.1007/bf00307532>
- Moorkamp, M. (2017). Integrating electromagnetic data with other geophysical observations for enhanced imaging of the Earth: A tutorial and review. *Surveys in Geophysics*, 38, 935–962. <https://doi.org/10.1007/s10712-017-9413-7>
- Mosenfelder, J. L., Asimow, P. D., Frost, D. J., Rubie, D. C., & Ahrens, T. J. (2009). The  $\text{MgSiO}_3$  system at high pressure: Thermodynamic properties of perovskite, postperovskite, and melt from global inversion of shock and static compression data. *Journal of Geophysical Research*, 114, B01203. <https://doi.org/10.1029/2008JB005900>
- Murase, T., & Mc Birney, A. R. (1973). Properties of some common igneous rocks and their melts at high temperatures. *Geological Society of America Bulletin*, 84, 3563–3592. [https://doi.org/10.1130/0016-7606\(1973\)84<3563:POSCIR>2.0.CO;2](https://doi.org/10.1130/0016-7606(1973)84<3563:POSCIR>2.0.CO;2)
- Nakajima, J., Hada, S., Hayami, E., Uchida, N., Hasegawa, A., Yoshioka, S., et al. (2013). Seismic attenuation beneath northeastern Japan: Constraints on mantle dynamics and arc magmatism. *Journal of Geophysical Research*, 118, 5838–5855. <https://doi.org/10.1002/2013jb010388>
- Nakajima, J., Takei, Y., & Hasegawa, A. (2005). Quantitative analysis of the inclined low-velocity zone in the mantle wedge of northeastern Japan: A systematic change of melt-filled pore shapes with depth and its implications for melt migration. *Earth and Planetary Science Letters*, 234, 59–70. <https://doi.org/10.1016/j.epsl.2005.02.033>
- Nakamura, H., Iwamori, H., & Kimura, J. I. (2008). Geochemical evidence for enhanced fluid flux due to overlapping subducting plates. *Nature Geoscience*, 1, 380–384. <https://doi.org/10.1038/ngeo200>

- Nakao, A., Iwamori, H., & Nakakuki, T. (2016). Effects of water transportation on subduction dynamics: Roles of viscosity and density reduction. *Earth and Planetary Science Letters*, 454, 178–191. <https://doi.org/10.1016/j.epsl.2016.08.016>
- Nishimoto, S., Ishikawa, M., Arima, M., Yoshida, T., & Nakajima, J. (2008). Simultaneous high P-T measurements of ultrasonic compressional and shear wave velocities in Ichino-megata mafic xenoliths: Their bearings on seismic velocity perturbations in lower crust of northeast Japan arc. *Journal of Geophysical Research*, 113, B12212. <https://doi.org/10.1029/2008JB005587>
- O'Connell, R. J., & Budiansky, B. (1974). Seismic velocities in dry and saturated cracked solids. *Journal of Geophysical Research*, 79(35), 5412–5426.
- Ogawa, Y., Ichiki, M., Kanda, W., Mishina, M., & Asamori, K. (2014). Three-dimensional magnetotelluric imaging of crustal fluids and seismicity around Naruko volcano, NE Japan. *Earth, Planets and Space*, 66, 158. <https://doi.org/10.1186/s40623-014-0158-y>
- Okada, T., Matsuzawa, T., Nakajima, J., Uchida, N., Yamamoto, M., Hori, S., et al. (2014). Seismic velocity structure in and around the Naruko volcano, NE Japan, and its implications for volcanic and seismic activities. *Earth, Planets and Space*, 66, 114. <https://doi.org/10.1186/1880-5981-66-114>
- Osanai, Y. (1985). Geology and metamorphic zoning of the main zone of the Hidaka metamorphic belt in the Shizunai River region, Hokkaido. *Journal of Geological Society of Japan*, 91, 259–278. <https://doi.org/10.5575/geosoc.91.259>
- Pearce, J. A., Stern, R. J., Bloomer, S. H., & Fryer, P. (2005). Geochemical mapping of the Mariana arc-basin system: Implications for the nature and distribution of subduction components. *Geochemistry, Geophysics, Geosystems*, 6, Q07006. <https://doi.org/10.1029/2004GC000895>
- Pommier, A., Gaillard, F., Pichavant, M., & Scaillet, B. (2008). Laboratory measurements of electrical conductivities of hydrous and dry Mount Vesuvius melts under pressure. *Journal of Geophysical Research*, 113, B05205. <https://doi.org/10.1029/2007JB005269>
- Pommier, A., & Le-Trong, E. (2011). "SIGMELTS": A web portal for electrical conductivity calculations in geosciences. *Computers & Geosciences*, 37(9), 1450–1459. <https://doi.org/10.1016/j.cageo.2011.01.002>
- Punturo, R., Kern, H., Cirrincione, R., Mazzoleni, P., & Pezzino, A. (2005). P- and S-wave velocities and densities in silicate and calcite rocks from the Peloritani Mountains, Sicily (Italy): The effect of pressure, temperature and the direction of wave propagation. *Tectonophysics*, 409, 55–72. <https://doi.org/10.1016/j.tecto.2005.08.006>
- Quist, A. S., & Marshall, W. L. (1968). Electrical conductances of aqueous sodium chloride solutions from 0 to 800° and at pressures to 4000 bars. *The Journal of Physical Chemistry*, 72(2), 684–703. <https://doi.org/10.1021/j100848a050>
- Reynard, B., Mibe, K., & Van de Moortèle, B. (2011). Electrical conductivity of the serpentised mantle and fluid flow in subduction zones. *Earth and Planetary Science Letters*, 307(3), 387–394. <https://doi.org/10.1016/j.epsl.2011.05.013>
- Rigden, S. M., Ahrens, T. J., & Stolper, E. M. (1989). High-pressure equation of state of molten anorthite and diopside. *Journal of Geophysical Research*, 94, 9508–9522. <https://doi.org/10.1029/JB094iB07p09508>
- Rivers, M. L., & Carmichael, I. S. E. (1987). Ultrasonic studies of silicate melts. *Journal of Geophysical Research*, 92, 9247–9270. <https://doi.org/10.1029/JB092iB09p09247>
- Sakuma, H., & Ichiki, M. (2016a). Density and isothermal compressibility of supercritical H<sub>2</sub>O-NaCl fluid: Molecular dynamics study from 673 to 2000 K, 0.2 to 2 GPa, and 0 to 22 wt% NaCl concentrations. *Geofluids*, 16(1), 89102. <https://doi.org/10.1111/gfl.12138>
- Sakuma, H., & Ichiki, M. (2016b). Electrical conductivity of NaCl-H<sub>2</sub>O fluid in the crust. *Journal of Geophysical Research: Solid Earth*, 121(2), 577–594. <https://doi.org/10.1002/2015JB012219>
- Seno, T., & Kirby, S. H. (2014). Formation of plate boundaries: The role of mantle volatilization. *Earth-Science Reviews*, 129, 85–99. <https://doi.org/10.1016/j.earscirev.2013.10.011>
- Sibson, R. H. (2009). Rupturing in overpressured crust during compressional inversion—The case from NE Honshu, Japan. *Tectonophysics*, 473, 404–416. <https://doi.org/10.1016/j.tecto.2009.03.016>
- Sinmyo, R., & Keppler, H. (2017). Electrical conductivity of NaCl-bearing aqueous fluids to 600°C and 1 GPa. *Contribution to Mineralogy and Petrology*, 172, 4. <https://doi.org/10.1007/s00410-016-1323-z>
- Stesky, R. M., & Brace, W. F. (1973). Electrical conductivity of serpentinized rocks to 6 kilobars. *Journal of Geophysical Research*, 78(32), 7614–7621. <https://doi.org/10.1029/jb078i032p07614>
- Stixrude, L., & Bukowinski, M. S. T. (1990). Fundamental thermodynamic relations and silicate melting with implications for the constitution of D. *Journal of Geophysical Research*, 95, 19311–19325. <https://doi.org/10.1029/JB095iB12p19311>
- Takei, Y. (2002). Effect of pore geometry on  $V_p/V_s$ : From equilibrium geometry to crack. *Journal of Geophysical Research*, 107(B2), 2043. <https://doi.org/10.1029/2001JB000522>
- Takei, Y. (2005). A review of the mechanical properties of solid-liquid composites. *Journal of Geography (Chigaku Zasshi)*, 114, 901–920. (in Japanese with English abstract). [https://doi.org/10.5026/jgeography.114.6\\_901](https://doi.org/10.5026/jgeography.114.6_901)
- ten Grotenhuis, S. M., Drury, M. R., Spiers, C. J., & Peach, C. J. (2005). Melt distribution in olivine rocks based on electrical conductivity measurements. *Journal of Geophysical Research*, 110, B12201. <https://doi.org/10.1029/2004JB003462>
- The MELT Seismic Team. (1998). Imaging the deep seismic structure beneath a mid-ocean ridge: The MELT Experiment. *Science*, 280, 1215–1218. <https://doi.org/10.1126/science.280.5367.1215>
- Ueki, K., & Iwamori, H. (2016). Density and seismic velocity of hydrous melts under crustal and upper mantle conditions. *Geochemistry, Geophysics, Geosystems*, 17, 1799–1814. <https://doi.org/10.1002/2015GC006242>
- Wada, N., Horiochi, N., Wang, W., Hiyama, T., Nakamura, M., Nagai, A., & Yamashita, K. (2012). Electrical conduction and polarization of calcite single crystals. *Physics and Chemistry of Minerals*, 39, 761–768. <https://doi.org/10.1007/s00269-012-0530-z>
- Wagner, W., & Prüß, A. (2002). The IAPWS formulation 1995 for the thermodynamic properties of ordinary water substance for general and scientific use. *Journal of Physical and Chemical Reference Data*, 31, 387–535. <https://doi.org/10.1063/1.1461829>
- Wang, D., Li, H., Yi, L., & Shi, B. (2005). The electrical conductivity of upper-mantle rocks: Water content in the upper mantle. *Physics and Chemistry of Minerals*, 35, 157–162. <https://doi.org/10.1007/s00269-007-0207-1>
- Wang, D., Li, H., Yi, L., & Shi, B. (2008). The electrical conductivity of upper-mantle rocks: Water content in the upper mantle. *Physics and Chemistry of Minerals*, 35(3), 157–162. <https://doi.org/10.1007/s00269-007-0207-1>
- Wang, X.-Q., Schubnel, A., Fortin, J., David, E. C., Guégén, Y., & Ge, H.-K. (2012). High  $V_p/V_s$  ratio: Saturated cracks of anisotropy effects? *Geophysical Research Letters*, 39, L11307. <https://doi.org/10.1029/2012GL051742>
- Watanabe, T. (1993). Effects of water and melt on seismic velocities and their application to characterization of seismic reflectors. *Geophysical Research Letters*, 20(24), 2933–2936. <https://doi.org/10.1029/93gl03170>
- Watanabe, T. (2005). Electrical properties of rocks: A review. *Journal of Geography*, 114, 837–861. [https://doi.org/10.5026/jgeography.114.6\\_837](https://doi.org/10.5026/jgeography.114.6_837)
- Watanabe, T., & Kurita, K. (1993). The relationship between electrical conductivity and melt fraction in a partially molten simple system: Archie's law behavior. *Physics of the Earth and Planetary Interiors*, 78, 9–17. [https://doi.org/10.1016/0031-9201\(93\)90079-o](https://doi.org/10.1016/0031-9201(93)90079-o)

- Watanabe, T., Makimura, M., Kaiwa, Y., Desbois, G., Yoshida, K., & Michibayashi, K. (2019). Elastic wave velocity and electrical conductivity in a brine-saturated rock and microstructure of pores. *Earth, Planets and Space*, 71, 129. <https://doi.org/10.1186/s40623-019-1112-9>
- Webb, S. L. (1992). Low-frequency shear and structural relaxation in rhyolite melt. *Physics and Chemistry of Minerals*, 19, 240–245. <https://doi.org/10.1007/BF00202314>
- Wu, T. T. (1966). The effect of inclusion shape on the elastic moduli of a two-phase material. *International Journal of Solids and Structures*, 2, 1–8. [https://doi.org/10.1016/0020-7683\(66\)90002-3](https://doi.org/10.1016/0020-7683(66)90002-3)
- Yoshino, T., & Katsura, T. (2013). Electrical conductivity of mantle minerals: Role of water in conductivity anomalies. *Annual Review of Earth and Planetary Sciences*, 41, 605–628. <https://doi.org/10.1146/annurev-earth-050212-124022>
- Yoshino, T., Matsuzaki, T., Shatskiy, A., & Katsura, T. (2009). The effect of water on the electrical conductivity of olivine aggregates and its implications for the electrical structure of the upper mantle. *Earth and Planetary Science Letters*, 288, 291–300. <https://doi.org/10.1016/j.epsl.2009.09.032>